

LASER INTERFEROMETER GRAVITATIONAL WAVE OBSERVATORY
- LIGO -
CALIFORNIA INSTITUTE OF TECHNOLOGY
MASSACHUSETTS INSTITUTE OF TECHNOLOGY

Engineering Note	LIGO-E2400218-v4	2025/12/03
JAC final design document		
Masayuki Nakano		

Distribution of this document:

LIGO Scientific Collaboration

California Institute of Technology
LIGO Project, MS 100-36
Pasadena, CA 91125
Phone (626) 395-2129
Fax (626) 304-9834
E-mail: info@ligo.caltech.edu

Massachusetts Institute of Technology
LIGO Project, NW22-295
Cambridge, MA 02139
Phone (617) 253-4824
Fax (617) 253-7014
E-mail: info@ligo.mit.edu

LIGO Hanford Observatory
PO Box 159
Richland, WA 99352
Phone (509) 372-8106
Fax (509) 372-8137
E-mail: info@ligo.caltech.edu

LIGO Livingston Observatory
19100 LIGO Lane
Livingston, LA 70754
Phone (225) 686-3100
Fax (225) 686-7189
E-mail: info@ligo.caltech.edu

Contents

1 Relavant document	5
2 Overview	6
2.1 Background and Motivation	6
2.2 Block Diagram	6
2.3 Requirements	8
3 JAC Design Considerations	9
3.1 Jitter Attenuation	9
3.1.1 Jitter Expression	9
3.1.2 Output Jitter Estimation	10
3.2 Polarization Separation	10
3.3 JAC Design Candidates	12
3.3.1 Jitter Attenuation	13
3.3.2 Mispolarization effect	13
3.4 Conclusion	13
4 HAM1 layout	17
4.1 Overview	17
4.2 Seismic Isolation	17
4.3 Mode matching	20
4.3.1 Requirement for the mode mismatching	23
4.3.2 PSL to JAC	23
4.3.3 JAC to IMC	24
4.4 Thermal Lens of the EOM	27
4.5 Height Adjustment	30
4.6 Polarization Rotation	31
4.7 Viewport	32
4.8 Power Adjustment	32
4.9 Leakage Port from JAC	33
4.10 Stray Light Control	33

5 JAC Control Loop Design	35
5.1 Length Control	35
5.1.1 Modulation	35
5.1.2 Sensor	35
5.1.3 Actuator	35
5.1.4 Servo	36
5.1.5 Length fluctuation	36
5.1.6 Intensity noise due to residual length fluctuation	38
5.1.7 Phase noise due to residual length fluctuation	42
5.1.8 Slow control	42
5.1.9 Conclusion of the length control	42
5.2 Alignment control	44
6 In air table layout	45
6.1 Layout	45
6.2 Gouy phase telescope	45
6.3 High power beam dump	46
6.4 ALS Path	46
7 Risk Registry	46
7.1 JM misalignment	46
8 Open questions	49
8.1 Thermal effect of the JAC	50
8.2 Length fluctuation	50
9 Safety	50
9.1 Laser safety	50
10 Wiring	51
10.1 Analog circuit	51
10.2 CDS	51
10.3 HAM1 flange feedthrough	51

11 Vacuum compatibility	51
11.1 Cavity	51
11.2 Electronics	51
12 Test plan	51
12.1 Jitter attenuation	52
13 Installation plan	52
14	52

1 Relevant document

Jitter Attenuation Cavity(JAC)

- [T2400329](#) Jitter Attenuation Cavity document tree
- [E2400349](#) Jitter Attenuation Cavity Design Requirements Document
- [G2401650](#) Jitter Attenuation Cavity preliminary design report
- [L2400050](#) JAC weekly meeting note
- [D2400257](#) Schematic wiring diagram of JAC for O5
- parts list
- [T2400328](#) JAC optics list
- [T2400360](#) List of relevant circuits for the JAC

Pre-Mode Cleaner (PMC)

- [E1200491](#) aLIGO Pre-mode cleaner document tree
-

Others

- [E2400246](#): A+ EOM crystal thermal lensing test

Drawing package

- [D1600270](#): aLIGO, PSL, PreMode Cleaner, SPACER ASSY.

Interface control document

Laser noise requirement

- [T0900649](#) PSL final design document

HAM1 ISI

- [E2200105](#): HAM1 stack to HAM1-ISI: E2200105

Optical path

- [HAM1 optical path](#)
- [T2400151](#): PSL+ Preliminary Table Layout Investigation
- [E1300206](#): aLIGO HAM2 Layout for IO Auxiliary Optics

- [T2400151](#): PSL+ Preliminary Table Layout Investigation
- [D1201103](#): ISCT1 Optical Layout

Wiring

- [D1900511](#): O5 ISC/SQZ Wiring Diagram for Corner Station
- [D0902810](#): aLIGO SUS HAM 1-2 System Wiring Diagrams
- [D1900511](#): O5 ISC/SQZ Wiring Diagram for Corner Station
- [D1002704](#): Rack and Cable Tray Layout_LVEA_H1
- [G1400098](#): Rack and Cable Tray Layout_LVEA_L1
- [D1201121](#): LVEA Rack PSL-R2
- [D1001460](#): ISC R1
- [D1001425](#): ISC R2
- [D1001427](#): ISC C1-C4 (CER Rack Layout)
- [E1100591](#): RF Signal Distribution (Cabling)

Viewport and flange

- [T2300221](#): Post-O4 HAM1 Flange Layout Discussions
- [D1101714](#): ALIGO HIGH POWER WEDGED 6IN VIEWPORT ASSY

2 Overview

2.1 Background and Motivation

During the O4 run, input beam jitter was identified as one of the noise sources limiting detector sensitivity [1]. Jitter-induced noise appeared at both LLO and LHO in the 100 Hz–1 kHz band (Fig. 1). As the detectors approach the improved O5 sensitivity, this coupling is expected to become an even stronger sensitivity limiter. The dominant jitter source was traced to the PSL periscope [2]. To mitigate this contribution, we propose installing an optical filtering cavity—the Jitter Attenuation Cavity (JAC)—between the PSL and the IMC. By suppressing $\text{TEM}_{10/01}$ content, the JAC reduces beam jitter before it couples into the interferometer. Installation is planned in preparation for the O5 observation period.

2.2 Block Diagram

The JAC is installed in HAM1 between the PSL and the IMC. The PSL output beam is transmitted through the JAC to the IMC, while the reflected beam exits HAM1 toward ISCT1 (LLO) or IOT1 (LHO), where it is used to generate length and alignment control signals.

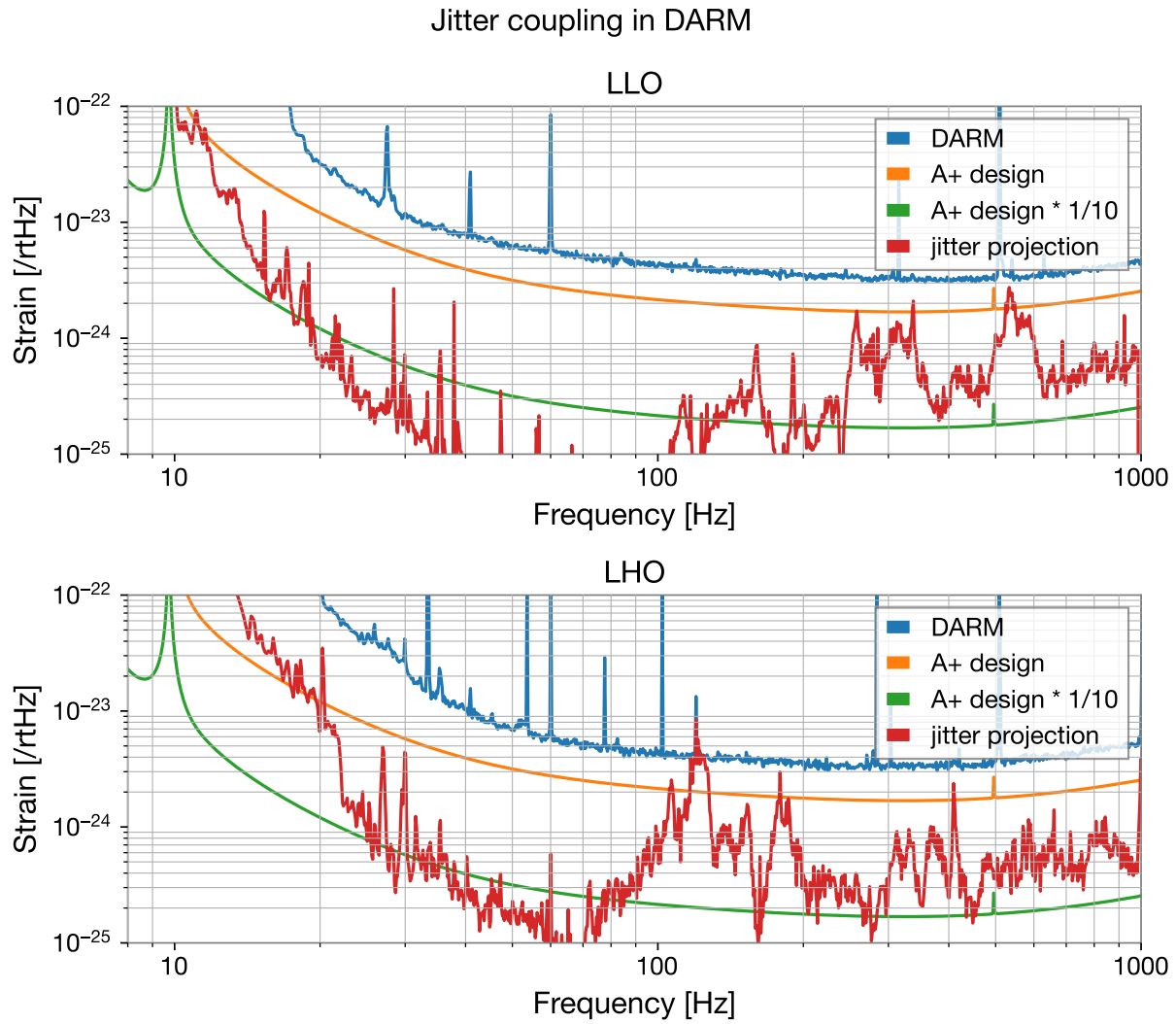


Figure 1: Jitter noise projection to DARM sensitivity. The orange trace shows the A+ target sensitivity. The green trace represents the jitter noise attenuation requirement, defined as the A+ target sensitivity multiplied by a safety factor of 10. Achieving 30 dB attenuation suppresses the projected jitter noise below this requirement.

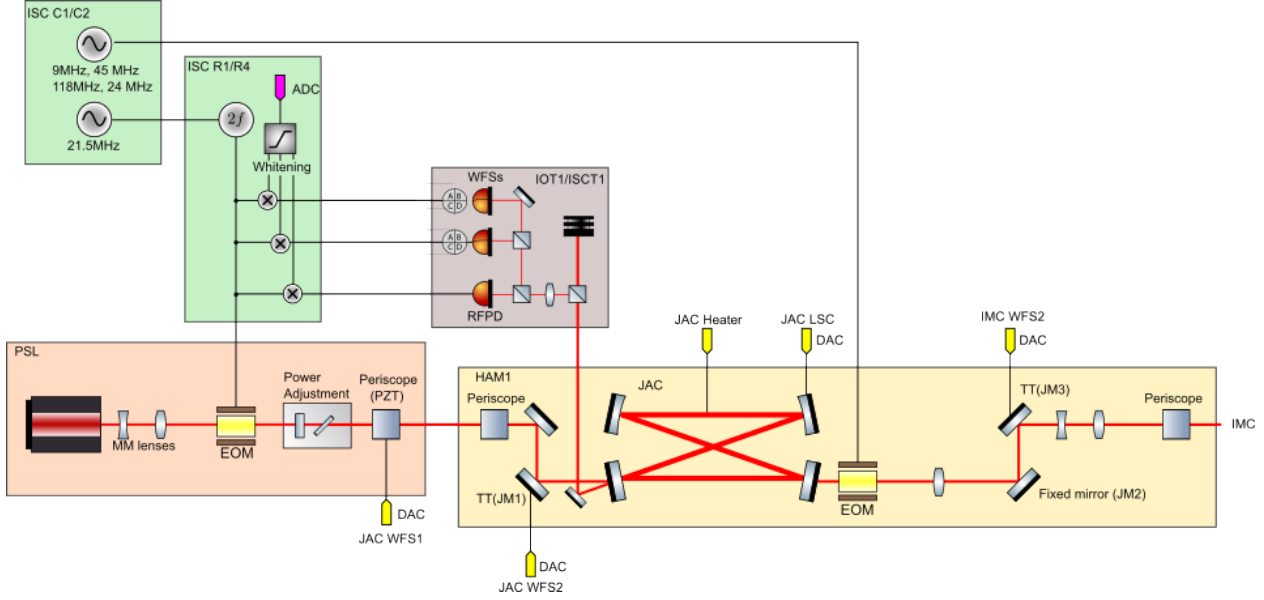


Figure 2: Block diagram of the JAC.

2.3 Requirements

The jitter attenuation requirement for the JAC is set to 30 dB. This value ensures that the projected jitter noise remains at least an order of magnitude below the A+ target sensitivity, assuming the same input jitter level and jitter coupling observed during O4. As illustrated in Fig. 1, the current jitter projection compared with the A+ design sensitivity (with a safety factor of 10, shown in green) indicates that achieving 30 dB attenuation is sufficient to bring the projected jitter noise below this requirement.

3 JAC Design Considerations

The JAC must provide sufficient suppression of the first-order spatial modes that carry beam jitter, while remaining compatible with the mechanical, optical, and operational constraints of HAM1. In this section, we evaluate three candidate cavity geometries—a triangular cavity, a optimized bow-tie cavity, and a direct replica of the aLIGO PMC—and compare their performance in terms of jitter attenuation, sensitivity to polarization effects, and practical implementability.

We begin by describing the mathematical formalism for beam jitter and the coupling of mirror motion into higher-order spatial modes. Using this model, the output jitter of each cavity design is estimated, including both the filtered residual jitter from the PSL and the jitter introduced by motion of the JAC optics themselves. We then analyze polarization-induced detuning, which differs significantly between triangular and bow-tie geometries, and assess the resulting contribution to relative intensity noise. Finally, we summarize the optical parameters of each configuration and discuss their expected performance.

As shown in the following subsections, although the triangular cavity provides an intrinsic advantage in suppressing polarization-induced detuning, all three candidate designs meet the jitter attenuation requirement.

The overall performance, combined with considerations of risk, availability, and ease of implementation, ultimately favors a JAC design identical to the current aLIGO PMC.

3.1 Jitter Attenuation

3.1.1 Jitter Expression

Before discussing the JAC geometry, we describe the mathematical representation of beam jitter. We assume that the laser propagates along the z -axis in the fundamental transverse electromagnetic mode (TEM_{00}). For simplicity, only the xz -plane is considered. A finite beam displacement Δx and angular deviation $\Delta\theta$ around the beam waist lead to coupling from the TEM_{00} mode into the TEM_{10} mode [?]:

$$E' = E_0 \left[\left(1 - \left(\frac{\Delta x}{w_0} \right)^2 - \left(\frac{\Delta\theta}{\alpha} \right)^2 \right) e_0 + \left(\frac{\Delta x}{w_0} + i \frac{\Delta\theta}{\alpha} \right) e_1 \right], \quad (1)$$

where E' is the electric field of the perturbed beam, E_0 is the input field amplitude, w_0 and α are the beam waist size and divergence angle, and e_0 and e_1 are the spatial profiles of the TEM_{00} and TEM_{10} modes, respectively. Jitter in the y -direction is described analogously using the TEM_{01} mode. Thus, beam jitter can be equivalently expressed as fluctuations in the amplitudes of the TEM_{10} and TEM_{01} modes.

Because the JAC acts as a spatial mode filter, suppressing higher-order modes, jitter attenuation is quantified by the suppression factor of the $\text{TEM}_{10/01}$ modes.

For the following discussion, we describe the first-order mode content generated by mirror

motion at a distance z from the beam waist. A rotation of the mirror by $\Delta\theta$ shifts the beam waist by $z\Delta\theta$ and introduces a tilt of $\Delta\theta$ around the waist. The resulting TEM₁₀ amplitude is

$$A_1 = \sqrt{\left(\frac{z\Delta\theta}{w_0}\right)^2 + \left(\frac{\Delta\theta}{\alpha}\right)^2} = \frac{kw_0}{\cos\eta(z)} \Delta\theta, \quad (2)$$

where k is the wavenumber and $\eta(z)$ is the Gouy phase at position z .

3.1.2 Output Jitter Estimation

In this subsection, we outline the method used to estimate the jitter noise at the JAC output. The output jitter consists of two contributions: (1) residual jitter after spatial filtering of the incident TEM_{10/01} modes by the JAC, and (2) jitter introduced by motion of the JAC itself.

We begin with the residual jitter. During O4, the dominant source of incident jitter was identified as motion of the upper mirror of the PSL periscope, across the entire observation band. The periscope mirror motion is reconstructed using the IMC WFS signals as witnesses and calibrated via PZT injection measurements [?]. Once the JAC geometry is fixed, the beam waist size and Gouy phase at the periscope location are determined. Assuming perfect mode matching between the PSL beam and the JAC eigenmode, the first-order mode content at the JAC input can be computed using Eq. (2). Combined with the TEM_{10/01} attenuation gain determined by the JAC geometry and finesse, the residual jitter at the JAC output can be estimated.

Next, we consider jitter introduced by motion of the JAC optics. The JAC is assumed to be mounted on the ISI table newly installed in HAM1. (Seismic isolation requirements and ISI performance are discussed in the next section.) The jitter contribution from JAC motion is computed from the ISI motion spectrum and the cavity parameters of the JAC. More detailed discussion of seismic isolation is provided in Sec. 4.2.

3.2 Polarization Separation

Odd-mirror cavities such as the triangular design exhibit polarization-dependent resonance frequencies, whereas even-mirror cavities such as the bow-tie design have resonances for the two linear polarizations that lie within a single cavity linewidth. When a beam with imperfect polarization is injected, this multi-resonant condition introduces an offset in the locking error signal and detunes the cavity. A detuned cavity converts residual laser-cavity frequency error into intensity fluctuations. From this viewpoint, the triangular cavity has an intrinsic advantage. In this subsection, we quantify this effect for comparison.

Assuming the JAC is critically coupled and operated close to resonance, the transmitted power for a purely p-polarized beam is

$$P_T^p(\xi) = \frac{P}{1 + \xi^2} \equiv PL(\xi), \quad (3)$$

where $L(\xi)$ is a normalized Lorentzian, P is the input laser power, and ξ is the detuning normalized by the half-width-half-maximum (HWHM). The cavity HWHM ω_c is related to the free spectral range (FSR) ω_{FSR} and finesse \mathcal{F} by $\omega_c = \omega_{\text{FSR}}/(2\mathcal{F})$.

If the resonance frequencies of two orthogonal polarizations differ by $\Delta\xi$, the transmitted power of the s-polarized beam is

$$P_T^s(\xi) = \frac{P}{1 + (\xi - \Delta\xi)^2} \equiv P L(\xi - \Delta\xi) \approx P \left[L(\xi) - \frac{dL}{d\xi}(\xi) \Delta\xi \right], \quad (4)$$

where the last expression assumes $|\Delta\xi| \ll 1$.

If the input beam has mixed polarization, with a rotation angle θ from p-polarization, then the transmitted power becomes

$$\begin{aligned} P_T(\xi) &= \cos^2 \theta P_T^p(\xi) + \sin^2 \theta P_T^s(\xi) \\ &\simeq P \left[L(\xi) - \frac{dL}{d\xi}(\xi) \Delta\xi \sin^2 \theta \right] \\ &\simeq P L(\xi - \Delta\xi \sin^2 \theta). \end{aligned} \quad (5)$$

Thus, the effective resonance peak shifts by $\Delta\xi \sin^2 \theta$. In practice, the cavity is locked to the maximum of the transmitted power with the Pound-Drever-Hall locking, so the operating point is detuned by this amount relative to the p-polarization resonance for a mixed-polarization input.

Under this locking condition, the transmitted electric field can be written as

$$\mathbf{E}_{\text{out}} = \sqrt{P_T^p(\Delta\xi \sin^2 \theta)} \mathbf{E}^p \cos \theta + \sqrt{P_T^s(\Delta\xi \cos^2 \theta)} \mathbf{E}^s \sin \theta, \quad (6)$$

where \mathbf{E}^p and \mathbf{E}^s are the unit polarization vectors for p and s, respectively. The output beam from the JAC is then injected into the Input Faraday Isolator (IFI). The IFI (and the IMC) preferentially transmits a single linear polarization and thus filters out the orthogonal component¹.

The JAC length control will also have a residual error $\delta\xi(t)$ in normalized detuning. Therefore, the power incident on the interferometer can be written as

$$\begin{aligned} P_{\text{IFO}}(t) &= P_T^p(\delta\xi(t) + \Delta\xi \sin^2 \theta) \\ &\simeq P \left[L(\Delta\xi \sin^2 \theta) + \frac{dL}{d\xi}(\Delta\xi \sin^2 \theta) \delta\xi(t) \right], \end{aligned} \quad (7)$$

where the second term in brackets represents the intensity noise coupled from the residual cavity length fluctuations.

The derivative of the Lorentzian evaluated at the detuned operating point is

$$\frac{dL}{d\xi}(\Delta\xi \sin^2 \theta) = \frac{-2\Delta\xi \sin^2 \theta}{[1 + (\Delta\xi \sin^2 \theta)^2]^2} \approx -2\Delta\xi \theta^2, \quad (8)$$

¹The p-polarization component at the JAC output is rotated into s-polarization by the HAM1 output periscope before injection into the IMC. Consequently, at the IMC and IFI the roles of “p” and “s” are effectively interchanged, but the analysis in terms of two orthogonal linear polarizations remains valid.

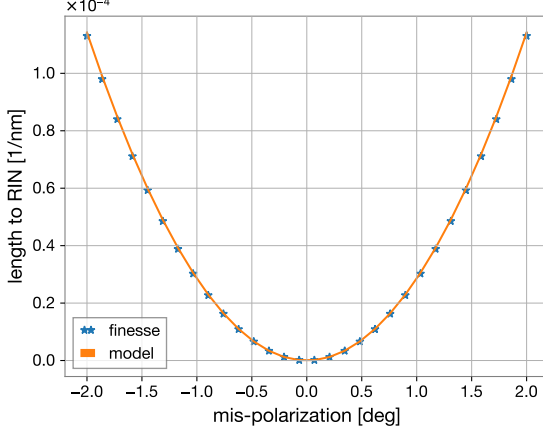


Figure 3: Transfer function from cavity length fluctuations to output relative intensity noise obtained from Eq. (10) and from FINESSE modeling.

where we used $\sin \theta \simeq \theta$ and $|\Delta\xi\theta^2| \ll 1$. This derivative gives the transfer function from residual JAC length noise to relative intensity noise (RIN) at the interferometer input.

The normalized detuning is related to the cavity length fluctuation δl by

$$\delta\xi = \frac{\delta l}{L_{\text{linewidth}}} = \frac{\delta l}{\lambda/(4\mathcal{F})} = \frac{4\mathcal{F}}{\lambda} \delta l, \quad (9)$$

where $L_{\text{linewidth}} = \lambda/(4\mathcal{F})$ is the cavity linewidth in the unit of length.

Combining Eqs. (8) and (9), the transfer function from cavity length fluctuations to RIN is

$$\begin{aligned} \frac{1}{P} \frac{dP}{dl} \Big|_\theta &= \frac{1}{P} \frac{dP}{d\xi}(\theta) \frac{\delta\xi}{\delta l} \simeq 2\Delta\xi\theta^2 \times \frac{4\mathcal{F}}{\lambda} \\ &= 2.9 \times 10^{-6} / \text{nm} \left(\frac{\Delta\xi}{0.01} \right) \left(\frac{\mathcal{F}}{125} \right) \left(\frac{1064 \text{ nm}}{\lambda} \right) \left(\frac{\theta}{1 \text{ deg}} \right)^2. \end{aligned} \quad (10)$$

This analytic model was validated using FINESSE [3]. As shown in Fig. 3, both approaches give consistent transfer functions.

3.3 JAC Design Candidates

Based on the discussion above, the output beam jitter and the relative intensity noise caused by the mispolarization were estimated for three different JAC configurations. The key parameters of each design candidate are summarized in Table 1.

Two classes of cavity geometries were considered: triangular and bow-tie. The overall cavity size is chosen to be comparable to the aLIGO PMC. Since spare PMC units are available, a direct replication of the current PMC design is considered as one candidate. In addition, because the PMC mirrors can be replaced without modifying the mechanical body, a bow-tie configuration using mirrors with different radii of curvature (RoC) was also evaluated. The RoC values are selected to optimize the Gouy phase and overlap with higher-order modes.

For the triangular cavity, dimensions similar to the PMC are chosen, with RoC values selected in the same manner as for the bow-tie design. The finesse is chosen such that the power density on the mirrors remains below 1 MW/cm^2 for 100 W of incident power. More detailed design considerations are discussed in [?].

3.3.1 Jitter Attenuation

The expected jitter attenuation performance is shown in Fig. 4. The newly designed cavities exhibit larger waist sizes than the PMC, and their higher achievable finesse yields stronger attenuation of $\text{TEM}_{10/01}$ modes. Between the two new designs, the bow-tie geometry places the mirrors farther from the beam waist, resulting in a larger beam size on the mirrors and allowing a higher finesse. Consequently, the bow-tie cavity achieves the highest attenuation among the three candidates. Nevertheless, all three configurations satisfy the jitter attenuation requirement.

3.3.2 Mispolarization effect

The resonance frequency splitting of the PMC caused by the birefringence has been reported to be $\Delta\xi \approx 0.01$ [?]. The estimated residual cavity-length fluctuation is $10^{-5}\text{--}10^{-4}$ nm in the observation band (Sec. 5.1.5), leading to RIN below 10^{-8} for a polarization misalignment of 5 deg. The corresponding estimation is shown in Fig. 5.

Two main mechanisms are expected to contribute to residual mis-polarization. The first is the finite extinction ratio of the thin-film polarizer at the downstream end of the PSL. Assuming a 60 dB extinction ratio, the resulting polarization rotation is on the order of 1 mrad (~ 0.05 deg). The second is imperfect alignment of the HAM1 input periscope, which rotates the beam polarization by 90 deg. A 1 deg misalignment of the periscope would introduce an additional ~ 1 deg of polarization error. Even under this conservative assumption, the resulting RIN remains below 10^{-8} , and is therefore not a significant noise source relative to the A+ target sensitivity.

From these considerations, we conclude that the bow-tie cavity is not disadvantageous with respect to polarization-induced detuning.

3.4 Conclusion

Although the triangular cavity provides an intrinsic advantage with respect to polarization-induced detuning, the resulting intensity noise is expected to be negligible compared to the A+ target sensitivity. From a practical standpoint, adopting the same design as the current aLIGO PMC offers significant benefits: it eliminates the need for a new mechanical design, reduces lead time, and allows immediate use of the existing spare PMC units while additional spares are fabricated.

The jitter attenuation performance can be improved by replacing the PMC mirrors, but the gain is limited to approximately 10 dB. Even without this modification, the existing PMC design provides sufficient attenuation to reduce the jitter noise well below the requirement, achieving the A+ target sensitivity with a safety factor of 10.

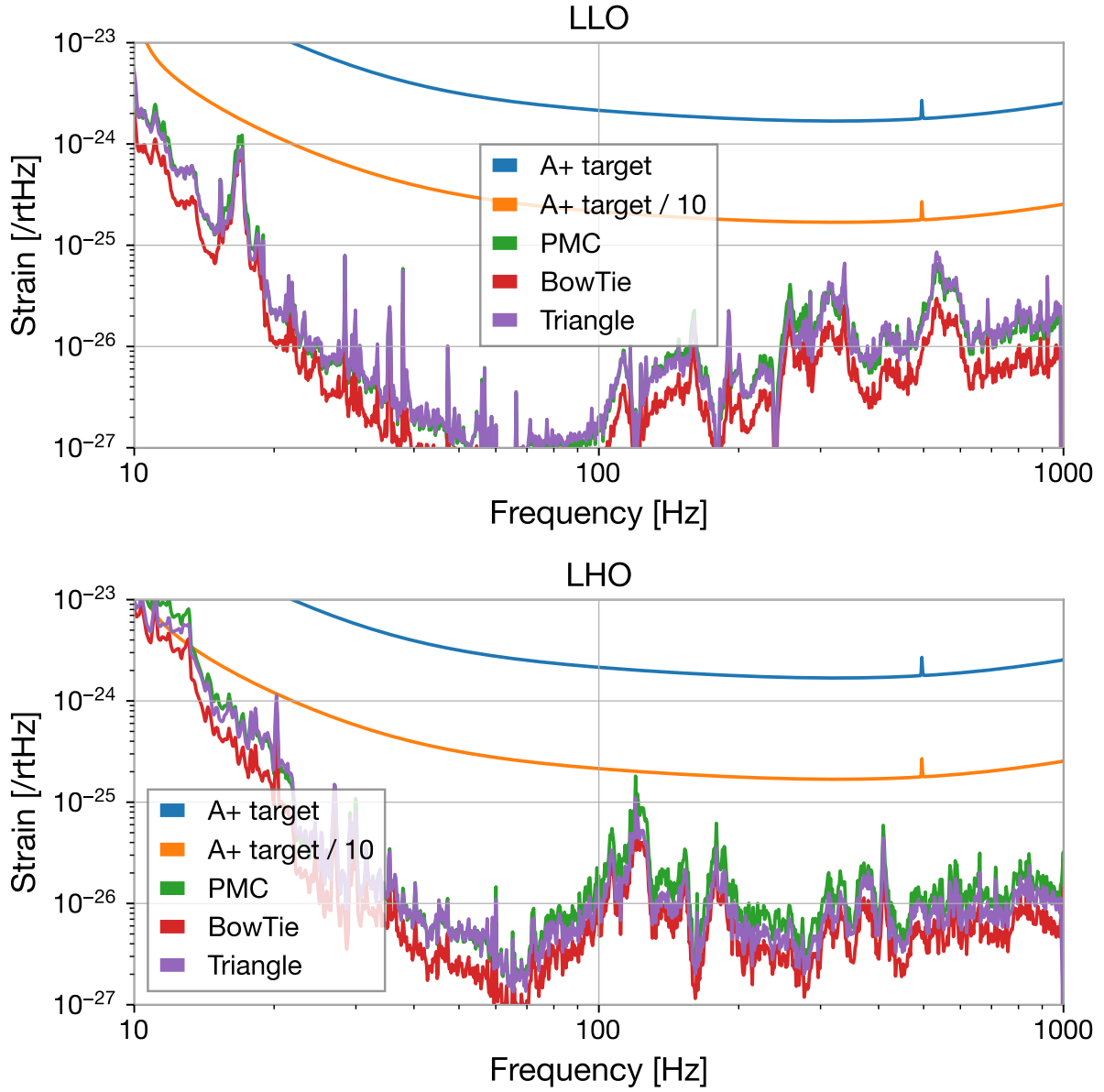


Figure 4: Projected jitter noise for the three JAC design candidates. The PMC curve corresponds to an exact replica of the current aLIGO PMC, while the bow-tie and triangular cavity designs are newly developed configurations. All three satisfy the jitter attenuation requirement, suppressing the jitter noise to more than an order of magnitude below the A+ target sensitivity.

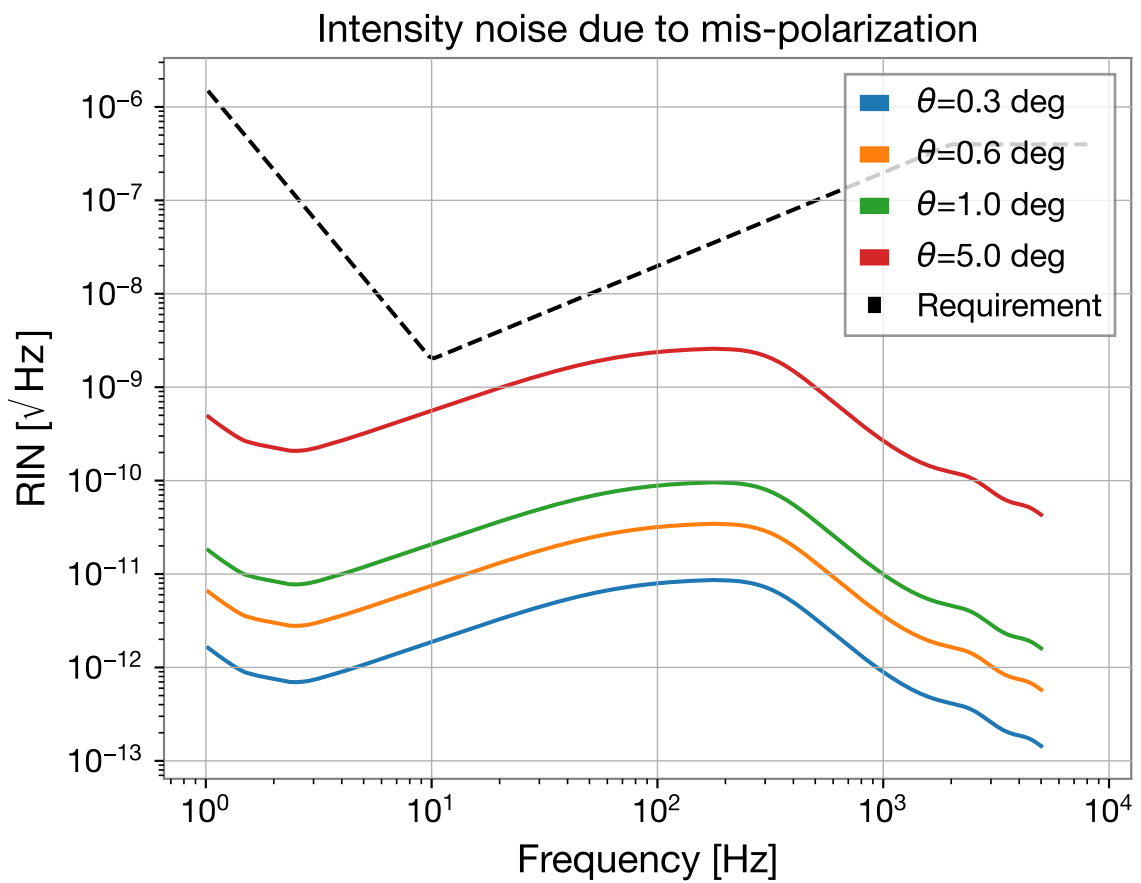


Figure 5: Relative intensity noise due to residual cavity-length fluctuations under mixed polarization. The estimation uses the length noise from Sec. 5.1.5 and assumes $\Delta\xi = 0.01$.

	Triangular	Bow Tie	Bow Tie (PMC)	
Dimension	$4'' \times 0.6$ m	$4'' \times 0.5$ m	$4'' \times 0.5$ m	
Mirrors	3	4	4	
Mirror curvature	5.0	8.5	3.0	m
Input/output reflectivity	2.25	0.98	2.48	%
Finesse	137	318	125	
Round-trip length	1.31	2.02	2.02	m
FSR	230	148	148	MHz
Waist size (x/y)	755/756	799/802	546/549	μm
Rayleigh range (x/y)	1.68/1.69	1.89/1.90	0.881/0.890	m
Divergence angle (x/y)	449/448	424/422	620/617	μrad
Round-trip Gouy phase (x/y)	222/42.2	57.0/56.8	101/100	deg
TEM10 (hor) attenuation	1.22	1.03	1.63	%
TEM01 (ver) attenuation	3.16	0.98	1.64	%

Table 1: Cavity parameters

Based on these considerations, we recommend employing a JAC that replicates the current PMC design exactly.

4 HAM1 layout

4.1 Overview

The HAM1 layout is shown in Fig. 6 and Fig. 7. The main components in HAM1 are the JAC, two tip-tilt steering mirrors [4], two periscopes [5], and a new in-vacuum EOM [6].

The input beam from the PSL is first adjusted in height by the upstream periscope to match the JAC input height. After passing through the JAC, the beam height is readjusted by the downstream periscope.

The angular actuators used for JAC and IMC alignment are the tip-tilt suspensions JM1 and JM3. JM1 is placed upstream of the JAC, and JM3 is located downstream. We previously considered installing an additional suspended mirror, JM2, after the JAC to provide another degree of freedom for IMC alignment control. However, due to space constraints, JM2 was implemented as a fixed mirror. For potential future upgrades, we retain the name “JM2,” although it no longer follows the standard naming convention.

The JAC reflection beam (JAC_REFL) is directed to ISCT1 [7] at LLO and to IOT1 [8] at LHO. ISCT1 is a shared table accommodating additional ISC paths such as ALS, REFL, and POP, whereas IOT1 is a new optical table located on the $-y$ side of HAM1 and is dedicated solely to the JAC_REFL path.

A new in-vacuum EOM is installed downstream of the JAC. Three mode-matching lenses are used to match the beam to the IMC eigenmode. A small fraction of the leakage light from the JAC is picked off and sent to a DC photodiode for transmission power monitoring.

4.2 Seismic Isolation

Seismic motion introduces angular jitter noise on the output beam, as described in Sec. 3.1.2. In this subsection, we evaluate the seismic-isolation performance of the HAM1 table by comparing the jitter induced by the ISI system planned for installation in the HAM1 chamber with that induced by the current HAM1 optical table. The present HAM1 table employs a three-stage seismic-isolation stack.

The table motion of the HAM1 ISI is assumed to be identical to that of the HAM2 ISI. The motion data were acquired on Aug. 07, 2023 at 04:00:00 UTC, using the channel `$(site)1:ISI-HAM2_BLND_GS13$(DoF)_IN1_DQ`. The HAM1 stack motion is modeled using measured values [9] below 20 Hz for horizontal motion and below 100 Hz for vertical motion. Above these frequencies, a $1/f^6$ roll-off is assumed. These motions are shown in Fig. 8. Although the stack provides stronger attenuation at high frequencies, the ISI offers significantly better isolation below 20 Hz (horizontal) and below 100 Hz (vertical).

For the output jitter noise calculation, the JAC design is assumed to be identical to the aLIGO PMC. The expected output jitter noise for each table configuration is shown in Fig. 9, and the corresponding projection to gravitational-wave sensitivity is presented in Fig. 10. In terms of raw table motion, the HAM1 stack provides slightly better isolation above ~ 20 Hz in the horizontal direction and shows comparable vertical isolation up to ~ 100 Hz, with the stack exhibiting better attenuation at higher frequencies. However,

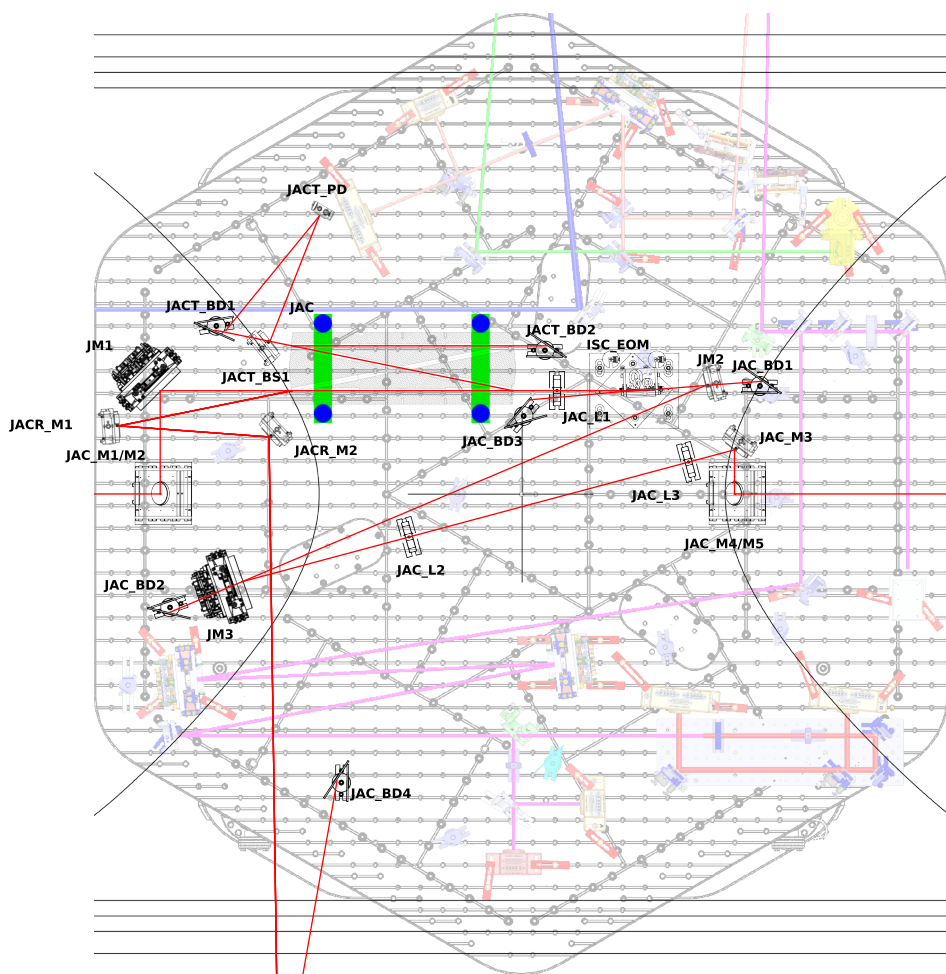


Figure 6: HAM1 layout design at LHO. The main components in HAM1 are the JAC, three tip-tilt steering mirrors, two periscopes, and an EOM.

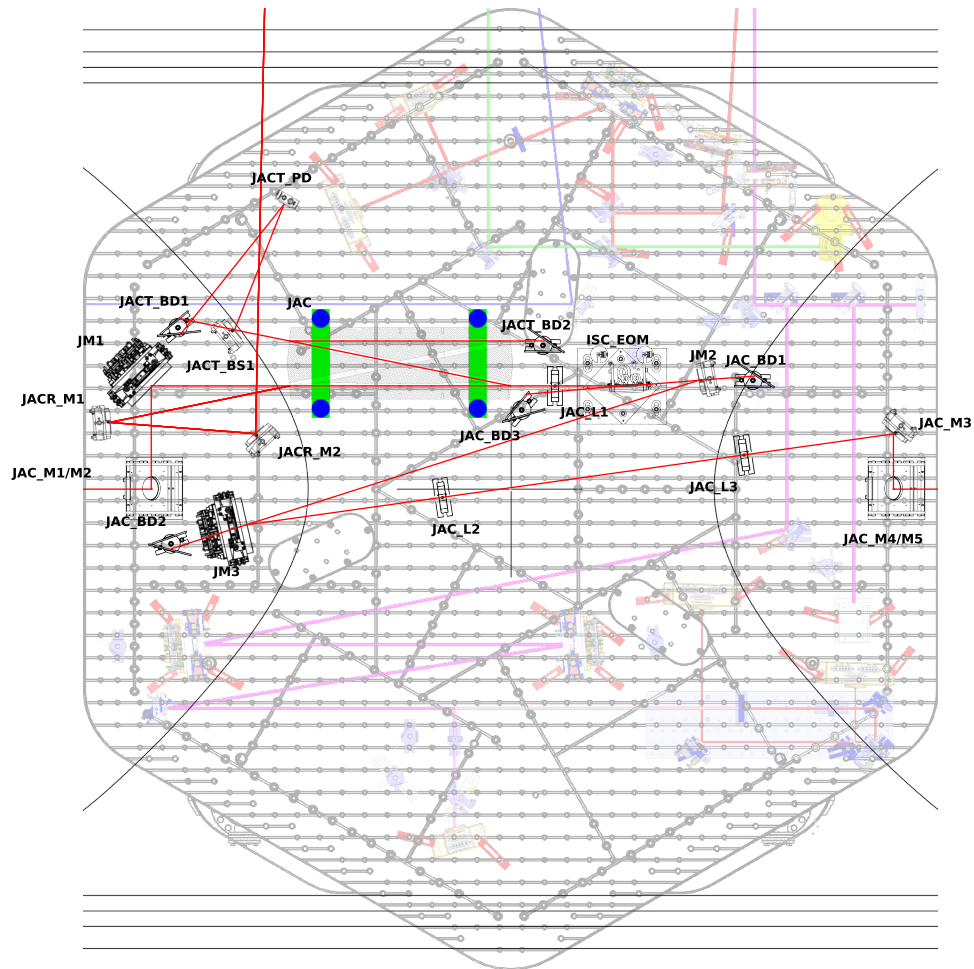


Figure 7: HAM1 layout design at LLO. Compared to the LHO design, the JAC_REFL beam path is directed in the opposite direction, toward ISCT1.

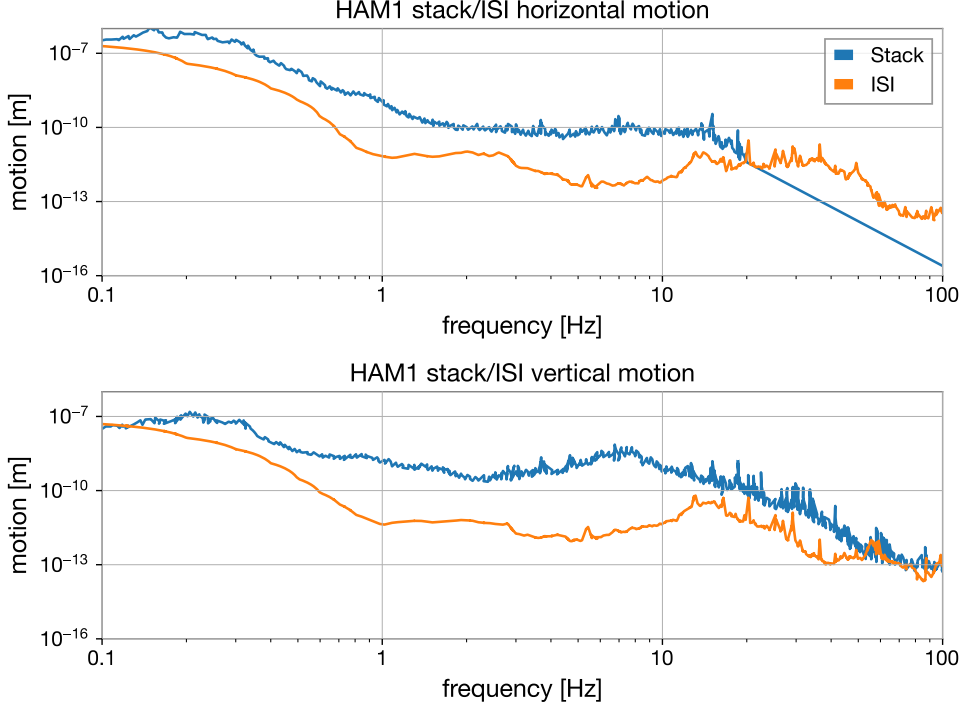


Figure 8: HAM1 table motion assumed in this study. Solid lines: measured HAM1 stack motion (horizontal below 20 Hz, vertical below 100 Hz; $1/f^6$ above these frequencies). Dashed lines: HAM2 ISI blend data used as a proxy for the planned HAM1 ISI.

when the jitter is projected onto DARM sensitivity, the ISI configuration outperforms the stack across the entire observation band. At high frequencies, this is because the dominant contribution arises from residual PSL jitter that the JAC cannot completely suppress, rendering the marginally better high-frequency stack isolation ineffective. At low frequencies, the ISI provides substantially superior seismic isolation, leading to significantly reduced jitter coupling. Consequently, the stack configuration results in noticeably larger jitter noise below ~ 30 Hz, in some cases approaching the A+ target sensitivity.

From the standpoint of seismic-isolation performance, achieving the A+ sensitivity across the full frequency band—particularly at low frequencies—requires the improved isolation provided by the ISI.

4.3 Mode matching

The HAM1 layout is set based on the mode matching to both the JAC and the IMC. In each case, lenses are used instead of curved mirrors; the lens specifications are given in [10, 11]. Mode matching to the JAC is performed in the PSL, while mode matching to the IMC is performed on HAM1.

Table coordinates for the PSL table, chambers, and ISI table follow [12, 13, 14, 15]. Because the PSL periscope height is not tabulated, the beam height is estimated from the HAM2 table coordinate and HAM2 periscope heights, assuming the PSL beam propagates horizontally.

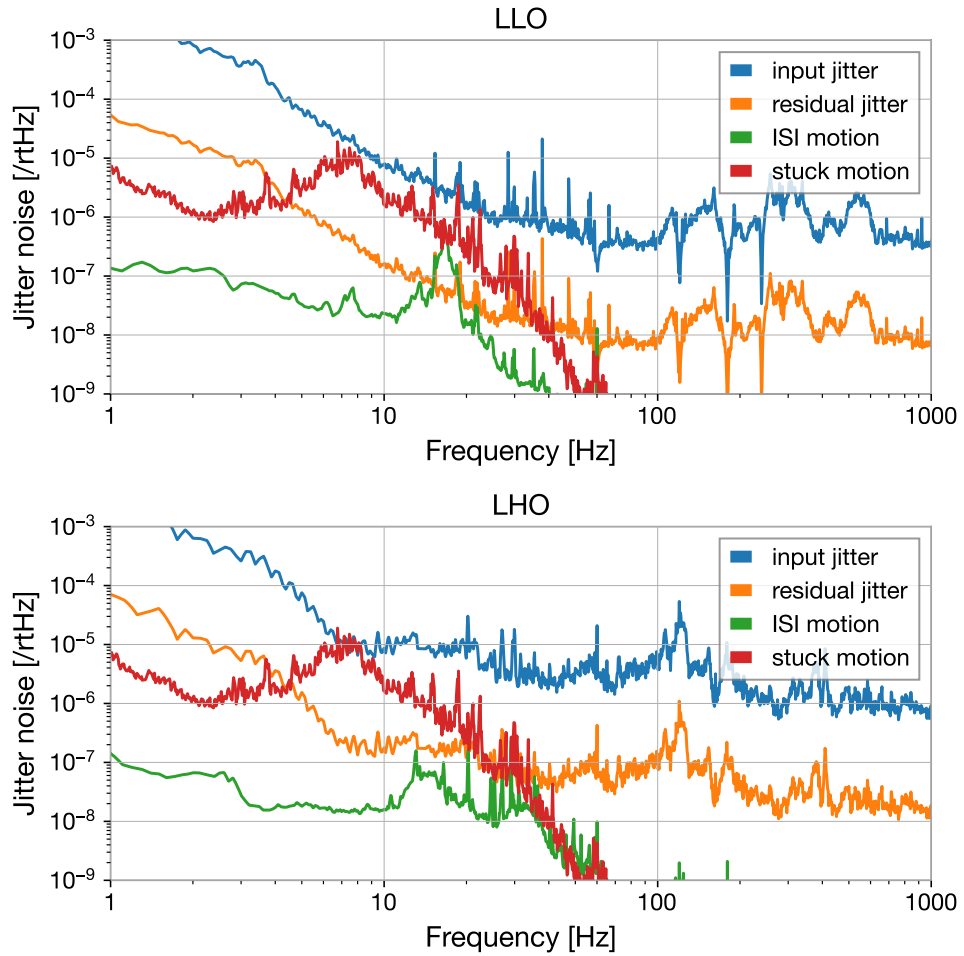


Figure 9: Expected jitter noise of the JAC output beam. The orange curve represents the residual input jitter (blue) after attenuation by the JAC. The red and green curves show the jitter introduced by the HAM1 stack and the ISI table motion, respectively.

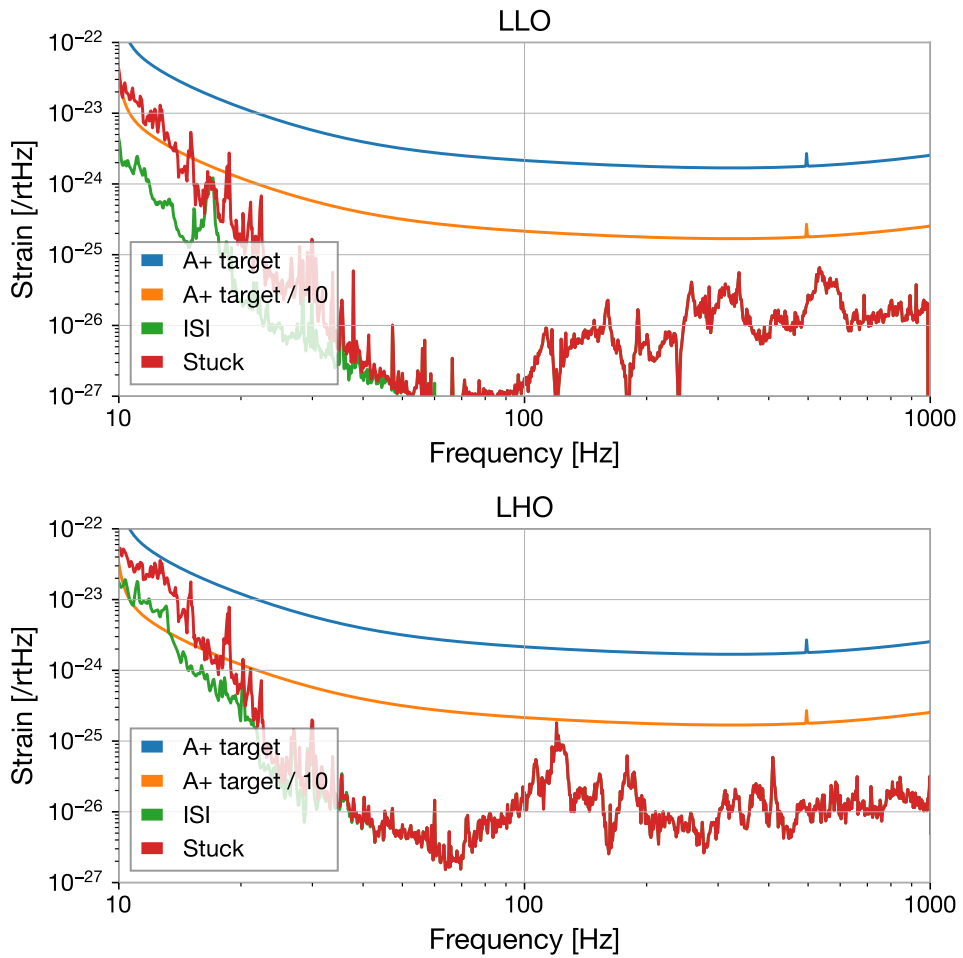


Figure 10: Projected jitter noise contribution to the gravitational-wave sensitivity for the ISI and HAM1 stack seismic isolation configurations.

4.3.1 Requirement for the mode mismatching

In the IMC REFL path, the reflected beam is attenuated by a 1000 ppm transmissive mirror and a 50/50 beam splitter before reaching the photodetector (PD). As a result, for a 100 W beam reflected from the IMC, approximately 50 mW of power is delivered to the PD.

The PD responsivity, accounting for the quantum efficiency (QE) of 0.96 and specified in the datasheet, is 0.83 A/W. Additionally, the shot noise intercept current—defined as the photocurrent at which shot noise equals the PD dark noise—is designed to be 2 mA for LSC RF photodetectors. This corresponds to an incident power of approximately 2.4 mW, which translates to a mode mismatching of 5%. Therefore, as long as the mode mismatching is below 5%, the noise contribution from the PD is dominated by its dark noise.

For the planned O5 operation, the EOM is designed to provide a modulation depth of approximately 20×10^{-3} rad. This modulation generates sidebands with a total power equivalent to about 2% of the mode mismatching. Considering this contribution, the PD noise remains dominated by its dark noise for mode mismatching up to 3%. From the perspective of IMC noise performance, setting the mode mismatching requirement to 2% appears reasonable.

In terms of power loss, the PSL itself is capable of delivering up to 110 W. To achieve the target of 100 W input to the interferometer, a mode mismatching of 2% is acceptable. Thus, this requirement balances both noise considerations and power delivery efficiency.

We don't have such strict requirement for the JAC mode-mismatching, since in any case the noise will be dominated by the JAC length motion, so we don't care so much about the PD sensing noise. But it's also reasonable to set same requirement for the JAC mode-mismatching from the view of the throughput.

4.3.2 PSL to JAC

The output beam from the PMC is injected into the EOM without any intervening lenses. This EOM provides the f_1/f_2 phase modulation, and although it will be relocated into HAM1 as discussed in the following section, the EOM is still required here for JAC sensing. Therefore, it is preferable to preserve the current beam size on the EOM. In addition, to avoid introducing new layout complications, the beam path from the EOM to the PSL periscope is kept identical to the present configuration.

Given these constraints, the first requirement for the JAC mode-matching design is the allowed region in which mode-matching lenses can be placed. The permissible longitudinal range begins 4 in. downstream of the PSL EOM and ends 4 in. upstream of the bottom mirror of the PSL periscope. The distance between these two points is approximately 2.2 m in the current layout, and this defines the allowed lens-placement interval. A second requirement comes from the desired JAC position: to realize a feasible HAM1 optical layout, the target waist location was set to 7.7–7.9 m downstream of the PMC.

For the mode-matching calculation, the code enumerates all possible lens-train combinations, places lenses on a coarse z -grid within the allowed region, and from each grid point runs a Nelder–Mead optimization to fine-tune the lens positions so that the resulting propagated beam waist matches the target. Any lens train achieving a mode mismatch below a defined

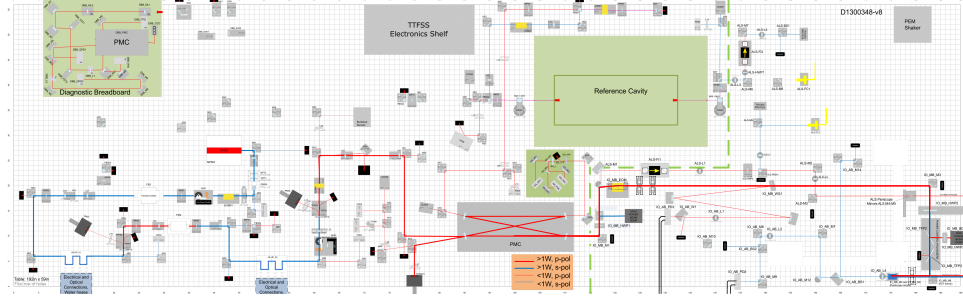


Figure 11: PSL layout in LLO showing the three mode-matching lenses on the PSL table (same configuration used at LHO). Two lenses are located close to the EOM, and the third lens is located just before the output periscope.

threshold is recorded, storing the lens positions, the resulting beam parameters, and the mismatch. The entire search is parallelized over all candidate trains and returns only the accepted solutions.

The PSL layout of the selected solutions satisfying these constraints are shown in Fig. 11, and the beam propagation is shown in Fig. 12. The final design uses three mode-matching lenses: IO_MB_L1, IO_MB_L2, and IO_MB_L3, with focal lengths of 0.56 m (convex; RoC 0.25 m), -0.33 m (concave; RoC 0.15 m), and 1.67 m (concave; RoC 0.75 m), respectively. Two lenses are located close to the EOM, and the third lens is located just before the output periscope. The Gouy-phase separations between the first two lenses and the third lens are approximately 20 degrees.

Figure 13 illustrates the sensitivity of the mode-matching performance to the lens positions. In these contour plots, the left panels show the waist-position shift (normalized by the Rayleigh range) as each lens is moved, the middle panels show the corresponding waist-size change, and the right panels show the total mode mismatch, given by the quadratic sum of the two. These results indicate that even if any of the lenses are displaced by ± 1 in., the resulting mode mismatch remains below 2%. Furthermore, the middle panels reveal that for lens pairs involving L1 and L3, the waist-size and waist-position variations are nearly orthogonal: translating L1 primarily changes the waist size, whereas translating L3 mainly shifts the waist position. This effective diagonalization of the two parameters demonstrates that the system permits relatively independent control of the waist size and waist location—greatly simplifying mode-matching alignment in practice.

4.3.3 JAC to IMC

The mode matching between the JAC and the IMC is performed on the HAM1 ISI table. Two steering mirrors are placed between the JAC and the IMC to form a zig-zag beam path, allowing for path-length adjustment without altering the HAM2 layout. The center-to-center separation between the HAM1 and HAM2 chambers is 2570 mm, and with an ISI table width of 1930 mm, the remaining edge-to-edge distance between the chambers is 640 mm. The beam path on HAM2 is fixed, and the distance from the HAM2 edge to the IMC waist

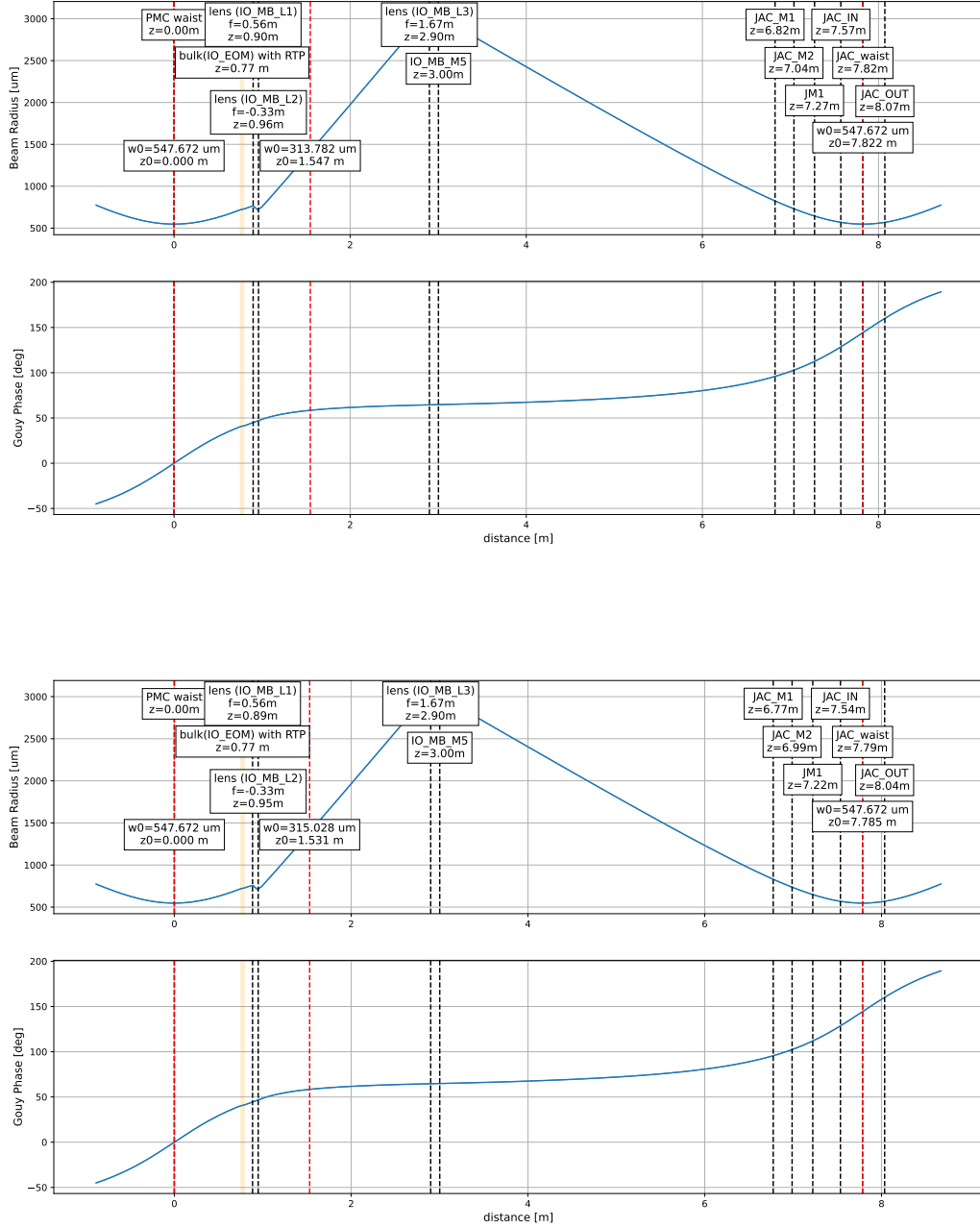


Figure 12: Beam propagation from the PSL to the JAC. Top: LHO layout. Bottom: LLO layout. In both cases, the first waist is that of the PMC, IO_MB_MX are the PSL mirrors defined in Fig. 11, and three mode-matching lenses are placed between the EOM and the PSL periscope.

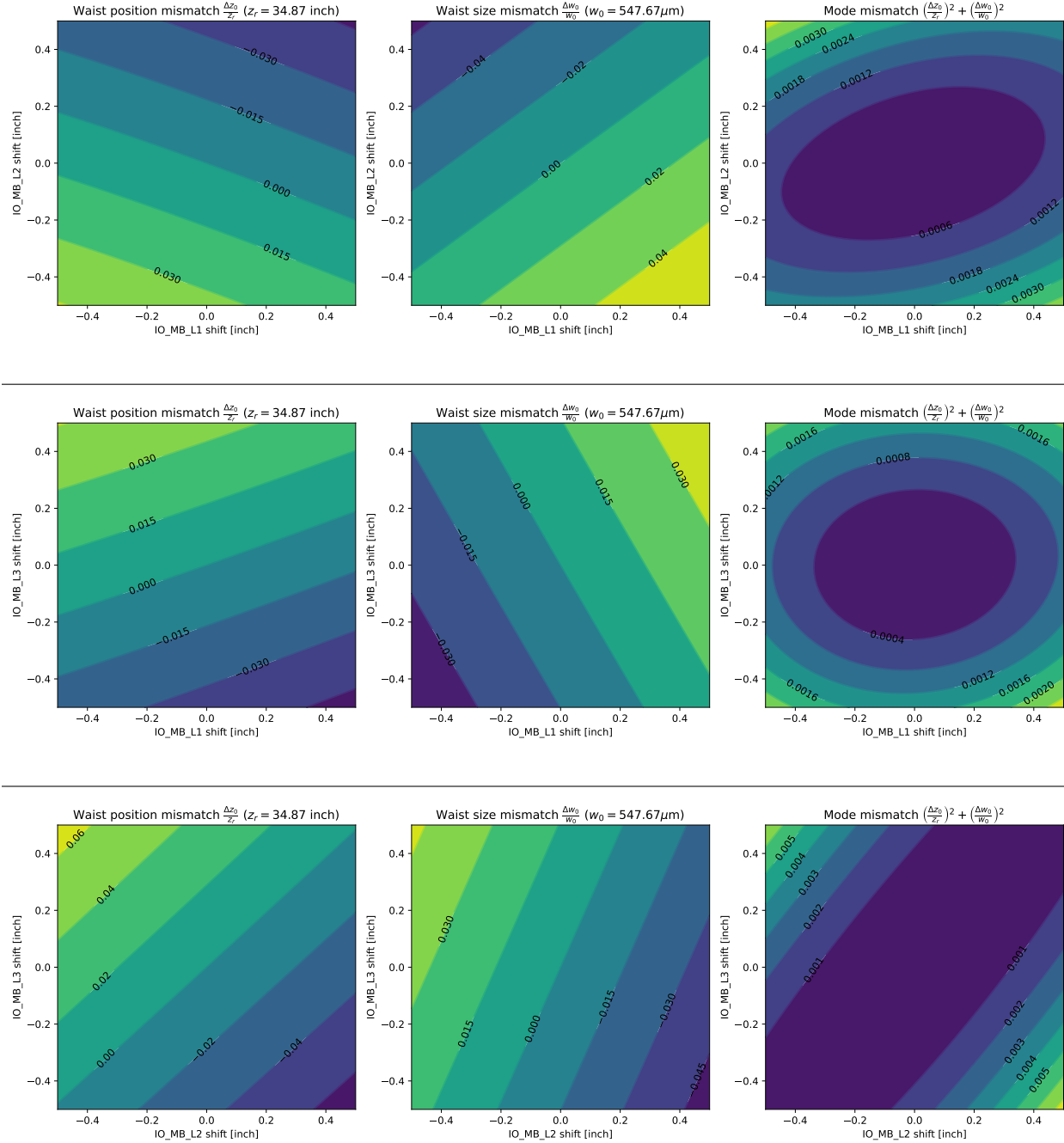


Figure 13: Contour maps showing the dependence of mode mismatch on the positions of each lens pair (IO_MB_L1–L2, IO_MB_L1–L3, and IO_MB_L2–L3; LLO configuration). The horizontal and vertical axes denote the longitudinal positions of the first and second lenses in each pair. Each column shows (left) waist-position error, (middle) waist-size error, and (right) total mode mismatch. Upper rows show normalized quantities; lower rows show absolute values. This plot is showing the solution for the LLO. The LHO has same trend.

position (located outside the IMC) is 1420 mm. By introducing a zig-zag path on HAM1, a total path length of approximately 3 m can be obtained, establishing the first constraint for the mode-matching design.

A second constraint arises from the IMC ASC requirements. Since there are no angular actuators on HAM2, it is advantageous to build an effective Gouy-phase telescope within HAM1 that provides both IMC mode matching and sufficiently large Gouy-phase separation for ASC actuation. In particular, the two steering mirrors that form the zig-zag beam path (JM2 and JM3) should ideally have a Gouy-phase separation close to 90 degrees, which diagonalizes the pitch and yaw sensing responses. In the present installation, however, only JM3 is equipped with a tip-tilt actuator, while JM2 remains a fixed mirror, so active ASC actuation cannot be performed using both mirrors. Even so, arranging the telescope such that these two Gouy phases are approximately orthogonal is beneficial for alignment robustness and provides a clear path toward future upgrades in which both mirrors may be made actuated.

One remaining uncertainty is the thermal lensing produced by the ISC EOM. This EOM replaces the PSL EOM and generates the modulation sidebands required for interferometer control. Its thermal-lensing behavior will be discussed in the next section. In this study, the circulating power on the EOM is assumed to be 100 W. The absorption coefficient is taken as a representative measured value of $\alpha = 500 \text{ ppm/cm}$, and we use an RTP thermo-optic coefficient of $dn/dT = 2.79 \times 10^{-6}/\text{K}$ and thermal conductivity of $\kappa = 3 \text{ W}/(\text{K m})$ [16].

Considering these constraints, the proposed mode-matching solution is shown in Fig. 14. The first lens (JAC_L1) is positioned immediately after the EOM to focus the beam near the first steering mirror (JM2), producing a Gouy-phase separation of about 100 degrees between JM2 and JM3. JAC_L1 is placed 0.38 m from the JAC output mirror, with a focal length and radius of curvature of 0.44 m and 0.25 m, respectively. Two additional lenses (with RoC values of 2 m and 1 m) are positioned between JM3 and the output periscope to complete the mode-matching telescope.

The mode-mismatch contour maps as functions of lens position are shown in Fig. 15. A key advantage of this solution is that the waist size is relatively insensitive to lens-position errors. Even with a $\pm 1 \text{ in.}$ displacement of any lens, the resulting waist-size variation is only $80 \mu\text{m}$ —approximately 4% of the IMC waist size—which corresponds to a mode mismatch of only 0.16% in power. The waist position is more sensitive than the waist size, but the tolerances remain practical: lens-placement accuracy of about 2 in. is sufficient to maintain a mode mismatch below 2%.

4.4 Thermal Lens of the EOM

Since the power on the ISC EOM will vary from 1 W to full power during the lock acquisition, the mode shape incident on the IMC will change due to the thermal lensing of the ISC EOM. To estimate this effect, the thermal lensing effect was tested for three samples of the RTP crystal [?].

Figure 16 summarizes the impact of the measured thermal lensing on the IMC mode matching. The left panel shows the thermal-lens optical power as a function of the injected optical

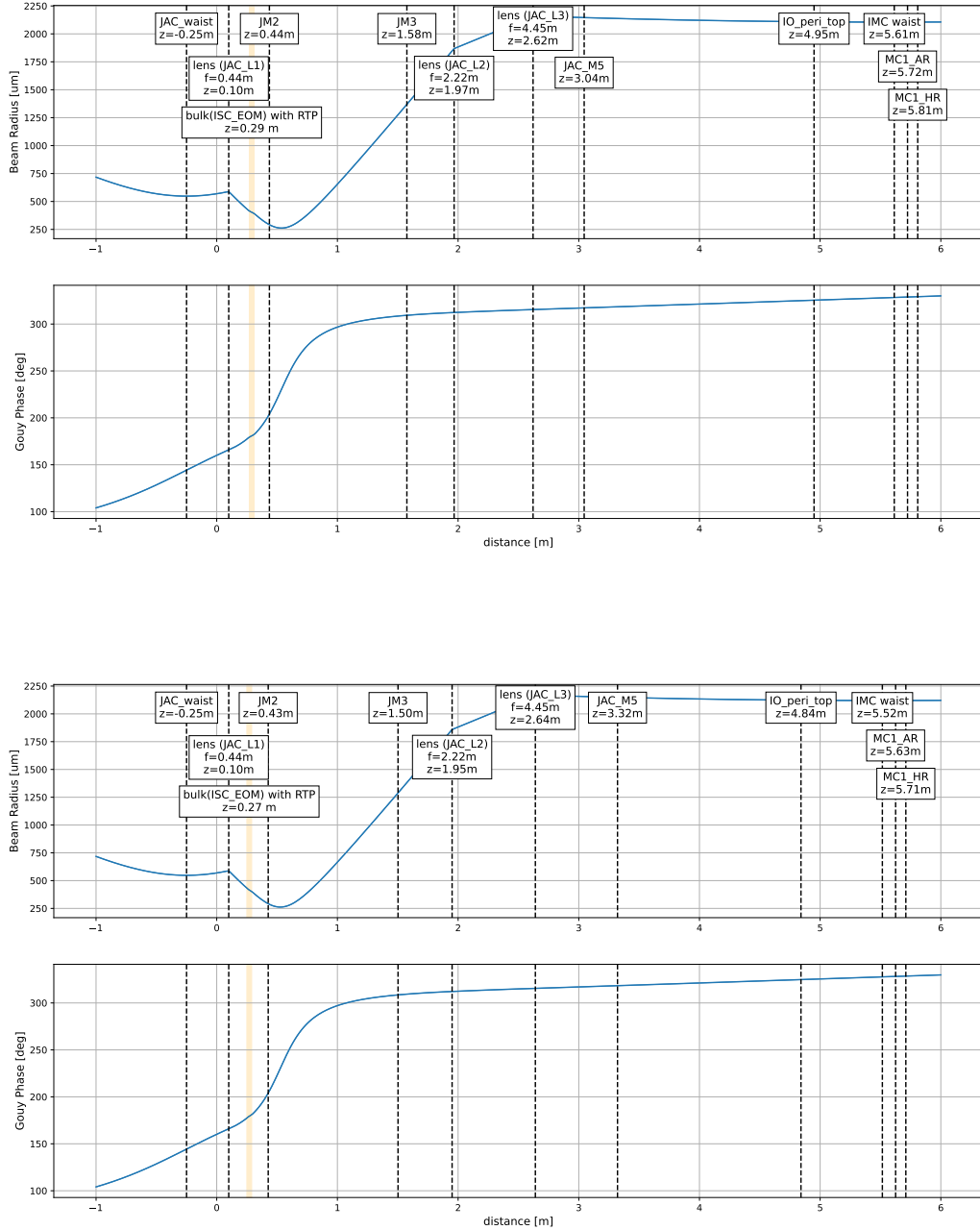


Figure 14: Beam propagation from the JAC to the IMC. Top: LHO layout. Bottom: LLO layout. In both cases, the first waist is the JAC waist, three lenses provide the IMC mode matching, JM2 and JM3 are the steering mirrors for the IMC alignment.

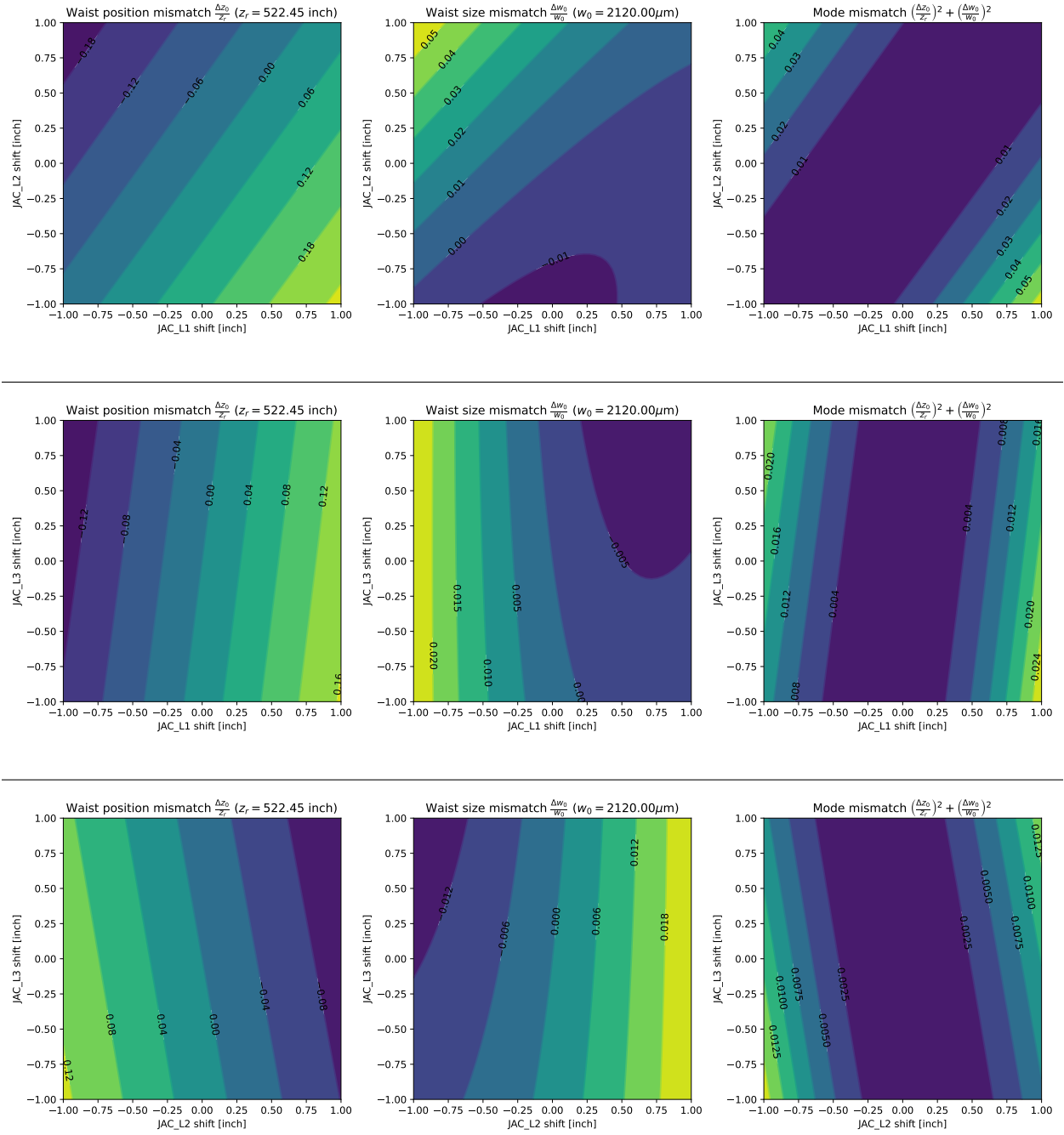


Figure 15: Mode-mismatch contour maps for all lens pairs (JAC_L1–JAC_L2, JAC_L1–JAC_L3, and JAC_L2–JAC_L3). For each plot, the horizontal and vertical axes represent the longitudinal positions of the first and second lenses in the pair. Columns show waist-position error (left), waist-size error (middle), and total mode mismatch (right); upper rows are normalized, and lower rows give absolute values.

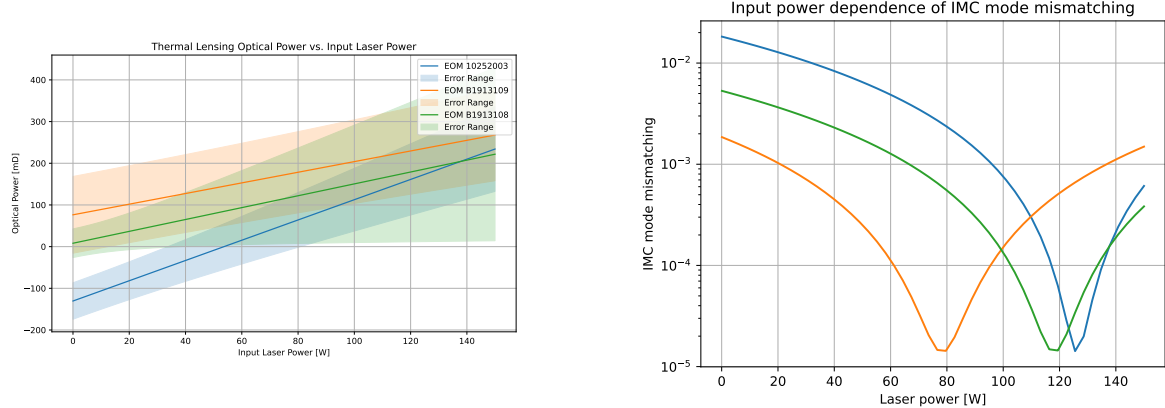


Figure 16: Left: thermal-lens optical power versus input power derived from the measured absorption of the three RTP samples. Right: IMC mode-mismatching versus input power for the same three samples.

power, computed from the measured absorption of the three RTP samples. Although the samples exhibit slightly different absorption coefficients, they all show that the thermal-lens strength increases from approximately 0 mD at low power to several hundred millidiopters over the 0–120 W range. Using these calculated thermal-lens powers, the corresponding IMC mode mismatch was then computed for each sample as a function of input power, as shown in the right panel. In other words, the right panel represents the IMC mode mismatch obtained when the EOM power is varied, with the thermal lens determined by the measured absorption of each crystal.

Once a reasonable mode-matching condition is established at low power, the additional degradation in mode matching induced by the evolving thermal lens remains small: across the 0–100 W operating range, the mode mismatch stays well below the 2% level, typically below 1%. This confirms that the EOM thermal lens does not pose a significant limitation for IMC mode matching under the expected operating conditions.

It is worth noting that there was a consideration to add a translation stage under the lens for IMC mode matching, enabling fine adjustment of the mode matching in vacuum. However, based on these discussion, we concluded that such a lens is unnecessary under these conditions.

4.5 Height Adjustment

The beam emerging from the PSL is currently approximately 12.5 in. above the surface of the ISI table [17, 18]. The beam height on HAM1, however, is set to 4 in. to match the JAC assembly and tip-tilt suspension height, requiring the beam to be lowered by about 8.5 in. upon entering HAM1. At the same time, the HAM2 optical layout imposes an additional constraint: the beam must pass above the input Faraday isolator (IFI) when propagating from HAM1 into HAM2. Consequently, after passing through the JAC, the output beam height must be raised back to approximately 12.5 in. to clear the IFI and interface properly with the HAM2 layout.

The first option for achieving the required height transition is to introduce periscopes on the HAM1 input and output paths, as illustrated in the proposed layout. This approach preserves the existing PSL beam height and requires only the addition of a corresponding periscope. Although it adds optical components, the complexity is modest, and the design leverages existing, well-tested periscope hardware already deployed in HAM2.

A second option is to reduce the beam height directly within the PSL. This would allow the PSL periscope to be shortened, thereby reducing input jitter. However, implementing this solution would require drilling a new feedthrough port in the PSL enclosure, fabricating a new PSL periscope, redesigning the HAM1 flange, and reconfiguring the PSL optical layout. These changes introduce substantial engineering effort, increased risk, and potential schedule impact.

A third possibility is to route the JAC beam through an alternative PSL–HAM1 port located at table height and currently used for the ALS beam (BF1 [19]). While this path is available, adopting it would still require PSL layout modifications, and the close proximity of the JAC and ALS beams could introduce unwanted scattering or cross-coupling between the two systems.

Given the significantly greater complexity associated with the second and third options, the first solution—using a pair of periscopes in HAM1 while keeping the existing PSL beam height unchanged—is the most practical and lowest-risk approach. The jitter impact is expected to be minimal, as a similar periscope is already present in HAM2, and the additional jitter introduced by the new periscopes is not expected to differ substantially.

For completeness, we note that other conceptual approaches were briefly considered. One idea was to construct a two-level optical table in HAM1 to accommodate both the current 12.5 in. PSL beam height and the 4 in. JAC height requirement without altering the PSL or HAM2 layouts. Another alternative was to redesign the entire JAC and surrounding HAM1 optics to operate at 12.5 in. throughout. Both approaches, however, introduce substantial mechanical complexity, require new suspension designs, and create additional potential sources of beam jitter. For these reasons, they were deemed impractical and were excluded from consideration.

In conclusion, we propose adopting the periscope-based height-adjustment scheme as the baseline design. While lowering the PSL beam height may offer advantages for future upgrades, the present solution provides the best balance of feasibility, optical performance, and implementation risk.

4.6 Polarization Rotation

The PSL output is *s*-polarized, as defined by the thin-film polarizer at the downstream end of the PSL enclosure, and the IMC is designed for *s* polarization. In contrast, the JAC (PMC) and the in-vacuum EOM operate with *p* polarization. Therefore, a 90° rotation of the polarization is required between the PSL and the JAC in order to satisfy the differing polarization requirements of the upstream and downstream subsystems.

As described in the previous section, a periscope is already required on HAM1 to reduce the PSL beam height to the ISI-table height. In addition to providing the required height

transition, the periscope geometry can also be used to rotate the output beam polarization. When the periscope is arranged so that the input and output beam axes are rotated by 90° , the local incidence planes of the two mirrors—and thus the definition of the s/p polarization basis—rotate by the same amount. As a result, the input s polarization is mapped to p polarization for the downstream JAC and EOM optics.

This approach provides a practical and low-risk method for achieving the required polarization rotation without introducing additional optical components. In particular, it avoids the need for a high-power, low-scatter half-wave plate, which would otherwise have to be placed in vacuum and would add complexity, cost, and potential scattering noise. For these reasons, the HAM1 periscope design intentionally departs from the HAM2 implementation—where no polarization rotation is introduced—and adopts a geometry that produces a controlled 90° beam-axis rotation. The detailed mechanical and optical design of the updated periscope is documented in [?].

The required accuracy of this polarization rotation is modest. As discussed in Sec. 3.3.2, the tolerance derived from length-noise-to-RIN coupling allows polarization misalignment of up to approximately 5° . Furthermore, the IMC throughput requirement of 2% corresponds to a polarization-rotation tolerance of $\text{arcsin}(\sqrt{0.02}) \approx 8^\circ$. The achievable mechanical alignment precision of the periscope is well within these limits, indicating that the periscope-based scheme comfortably satisfies all polarization-rotation requirements without the need for additional optics.

4.7 Viewport

The JAC reflected beam is routed from HAM1 to ISCT1 at LHO and to IOT1 at LLO. When the JAC loses lock, the full input power is reflected, and this entire power passes through the corresponding viewport. Therefore, the viewport must be capable of handling high optical power without introducing thermal deformation, scattering, or absorption-related damage.

From the layout constraints, viewport A1F5 [19] was selected for LLO and viewport A2F3 for LHO. These viewports are dedicated to the JAC_REFL beam path and are not shared with any other beam, which is advantageous for avoiding stray light, interference, or alignment conflicts with other subsystems.

The performance requirements for this viewport are similar to those for the IMC REFEL viewport and for the PSL-HAM1 injection viewport. For consistency and to minimize qualification effort, we propose using the same viewport type as those systems [19].

4.8 Power Adjustment

During lock acquisition, the output power from the PSL varies from a few watts up to 100 W. This power adjustment is performed using a half-wave plate (HWP) followed by a thin-film polarizer (TFP). In the current system, the HWP is mounted on a motorized rotation stage located downstream of the PSL, allowing remote control of the injected power.

During the design phase, we considered whether the power should continue to be adjusted in the PSL area, as in the current configuration, or whether the power-control optics should be

relocated downstream to HAM1, i.e., after the JAC. Locating the power-control mechanism in HAM1 would offer the benefit that both the JAC and the in-vacuum EOM would operate at constant optical power, potentially improving thermal stability. This was of particular interest because of the concern that the EOM’s thermal lens might introduce undesirable mode distortions.

However, implementing a motorized rotation stage inside the vacuum system would require a new mechanical design and fabrication effort, along with additional engineering risk. As discussed in Sec. 3.3.2 and in the thermal-lens analysis of Sec. 4.4, the thermal lensing of the EOM is sufficiently small across the expected operating power range, and the JAC is likewise expected to tolerate the power variation without significant thermal impact, based on prior experience with the PMC.

Considering these factors, we conclude that maintaining the existing power-adjustment scheme at the PSL is the most practical and reliable solution, and relocating the power-control optics to HAM1 is unnecessary.

4.9 Leakage Port from JAC

The power leaking from the JAC via mirrors other than the input and output couplers is designed to be sensed or dumped in vacuum. This approach prevents direct observation of the leakage beam with a camera; however, this is not a significant limitation, as the IMC REFL camera can serve as an effective diagnostic channel.

It is nevertheless worthwhile to consider the option of routing this leakage beam out of the chamber. One possible application is the ISS inner loop, which currently uses a photodetector monitoring the leak light from the PMC. Given the potential for excess noise originating from the JAC, relocating the ISS monitoring PD to one of the JAC output beams could reduce sensing noise and improve overall performance. Enabling such a configuration would require modifications to the ISCT1 or IOT1 layout and associated cabling. A similar argument could be made for the frequency-stabilization system, although the complexity of its optical path makes such changes more involved.

If leakage-beam extraction is implemented, the optical power levels must be considered. For a 100 W JAC input, the leakage power at these ports is expected to be on the order of 300 mW, which is too high to be sent directly to a photodetector. To reduce the power to a suitable level, we propose using an uncoated fused-silica laser window [20]. With a typical reflection of approximately 0.6%, the power incident on the PD would be reduced to about 1 mW, which is compatible with standard photodiodes [21].

4.10 Stray Light Control

Stray light in HAM1 will be managed using standard SLiC beam dumps. All expected secondary beams, including those discovered during in-vacuum alignment, will be captured using standard SLiC dumps [?], and no additional SLiC development is anticipated at this stage. In particular, the ghost beams generated by the steering mirrors and by the AR surfaces of the EOM will be terminated with these beam dumps, as indicated in the layout

diagrams in Figs. 6 and 7. In addition, a DLC-coated fused-silica plate (identical to those used in the SLiC beam dumps) will be mounted at the transmission port of each periscope to intercept any residual transmitted light.

The primary potential sources of stray light in this system are the viewport used for the JAC reflection beam and the high-power beam dump located on the ISCT1 table. With a few percent of mode mismatch, several watts of optical power may be incident on these components. While the backscattered light from these locations may not directly couple into the main interferometer beam path, its presence is nevertheless a concern due to the nearby POP and REFL photodiodes associated with the main ISC system. Scattered light from these elements could, in principle, couple into DARM through auxiliary degrees of freedom, and thus these locations must be treated as critical stray-light sources.

5 JAC Control Loop Design

5.1 Length Control

The Pound-Drever-Hall (PDH) method will be used for length control. The IO EOM located in the PSL will be used for the modulator, and the reflection from the JAC will be directed to the ISCT1/IOT1 and sense the signal with the LSC RFPD [22] located on the table. The digital servo will be used for the control. For the shot noise calculation, 2% of mode-mismatching is assumed.

5.1.1 Modulation

The modulation frequency is set to 43 MHz, which is twice the modulation frequency used for the PSL FSS reference cavity (21.5 MHz). This frequency was chosen because the IO EOM has a 45 MHz channel, and the modulation index at 43 MHz is relatively large, approximately 0.1 rad/V [23]. Additionally, generating the RF signal is straightforward using a frequency doubler [24]. The RF signal for modulation is taken directly from the distributor output, with a power level of 10 dBm, resulting in a modulation index of 0.01.

5.1.2 Sensor

The PD used to obtain the signal will be the LSC RFPD. The responsibility of the photodiode (Excelitas, C30642 [25]) is approximately 0.82 A/W, with a quantum efficiency (QE) of 0.96 at 1064 nm, and a transimpedance is around 200 ohms. The RF beat signal will be demodulated with LSC I/Q demodulator [26], which has the conversion gain of 22 dB Vpp/Vpp [27]. The injection power to the JAC is assumed as 100 W. The power reflected from the JAC and injected to the RFPD is adjusted with the HWP and PBS pair, and we assumed the 20mW injected into RFPD with the 100W JAC injection. The PD noise is calculated with 2 mA of shotnoise intercept current[28].

The beat signal amplitude of the reflected light can be written as

$$P(\xi) = 4P_{DC}J_0(\beta)J_1(\beta)\frac{\xi - \xi_0}{1 + (\xi - \xi_0)^2}, \quad (11)$$

where ξ is the normalized frequency by the half-width-half-maximum (HWHM) ξ_c , ξ_0 is the resonant frequency, $J_n(\xi)$ is the Bessel function, and β is the modulation index. The beat signal amplitude near resonance is approximately $4P_{DC}J_0(\beta)J_1(\beta)$. Thus, including the PD and I/Q demodulator parameters, the optical gain near the resonance can be calculated as 0.71 V/HWHM. The expected error signal calculated by Finesse is shown in Fig. 17.

5.1.3 Actuator

The actuator will use a PZT attached to the JAC. We assume the use of a Noliac PAHH-0013 (PI) PZT, which has a DC response of 0.41 $\mu\text{m}/200\text{V}$. This value was calculated from the calibration measurement reported in [29] and the DC gain 75 V/V of the PMC PZT driver. The high-voltage (HV) amplifier used to drive the PZT is [30], with a frequency response

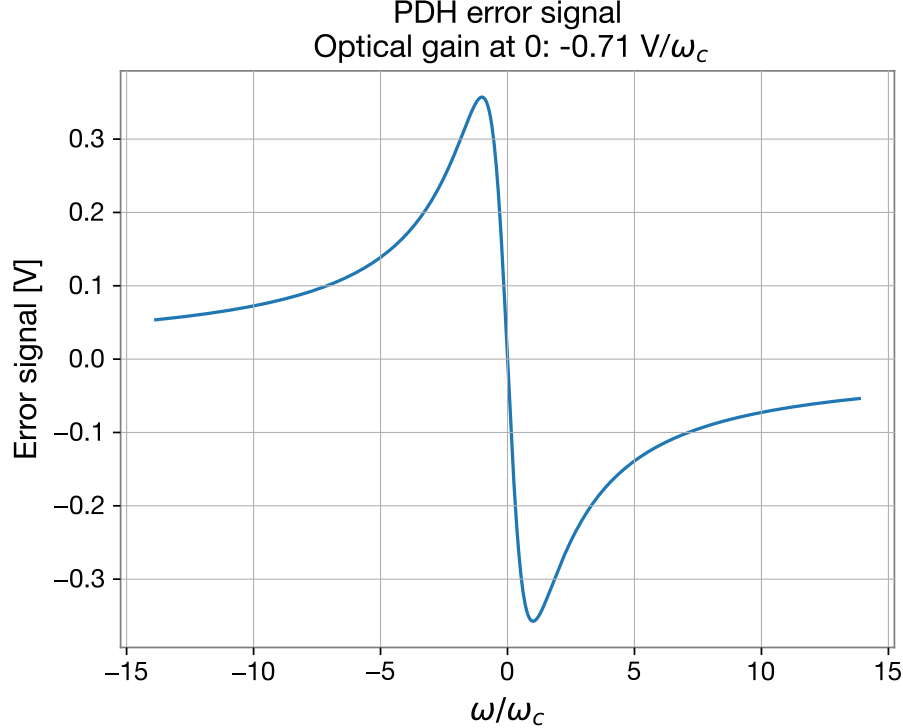


Figure 17: PDH signal at the IQ demodulator calculated by Finesse model.

characterized by poles at 1 Hz and 500 Hz, a zero at 15 Hz, and a DC gain of 30dB. The transfer function is shown in [31]

5.1.4 Servo

The control system will be implemented using a digital control system of CDS. Based on the data from T2000188, the phase delay caused by the CDS is expected to be approximately 300 μ sec, which corresponds to a delay of about 5 cycles at a sampling rate of 16 kHz. Since the document assumes a direct connection between the ADC and DAC, so we should consider additional phase delays caused by model dependencies. So, we assume a time delay of 500 μ sec, which corresponds to approximately 8 cycles. The achievable unity gain frequency (UGF) is determined by this phase delay.

The servo will be designed with a phase margin requirement of 30 degrees. Assuming a first-order integrator and a first-order boost below 50 Hz, the open-loop gain will have a slope of $1/f^2$ below 50 Hz and $1/f$ above 50 Hz. Considering the phase response, an optimal UGF of around 200 Hz is expected. The Bode plot of the resulting open-loop transfer function is shown in Fig. 18. The phase margin is 40 degree.

5.1.5 Length fluctuation

The length fluctuation of the JAC was estimated based on the current length fluctuation of the PMC. Fig. 19 shows the PMC control signal multiplied by the actuator efficiency (3.7 μ m/1000V). Since the PMC's length control bandwidth is in the kHz range, this serves as

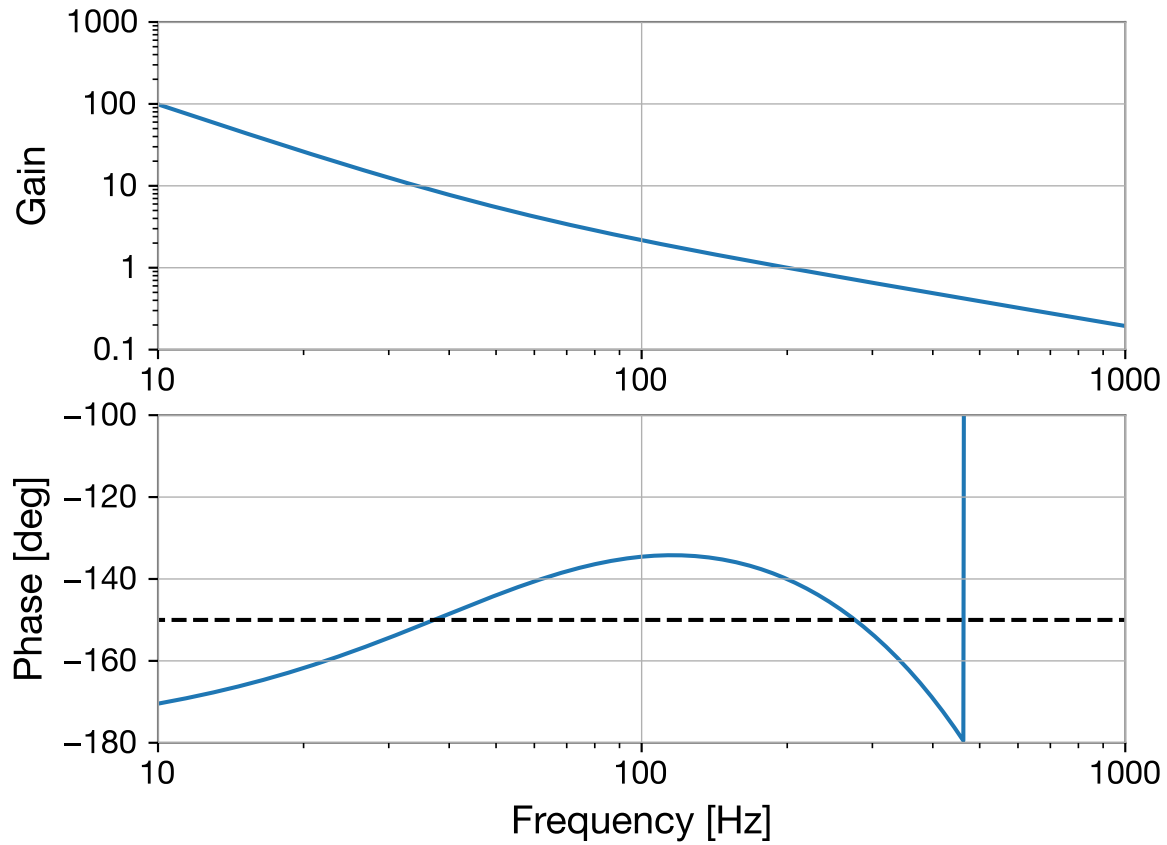


Figure 18: Open loop transfer function of the JAC LSC. Unity gain frequency is 200 Hz, and phase margin is 40 degrees.

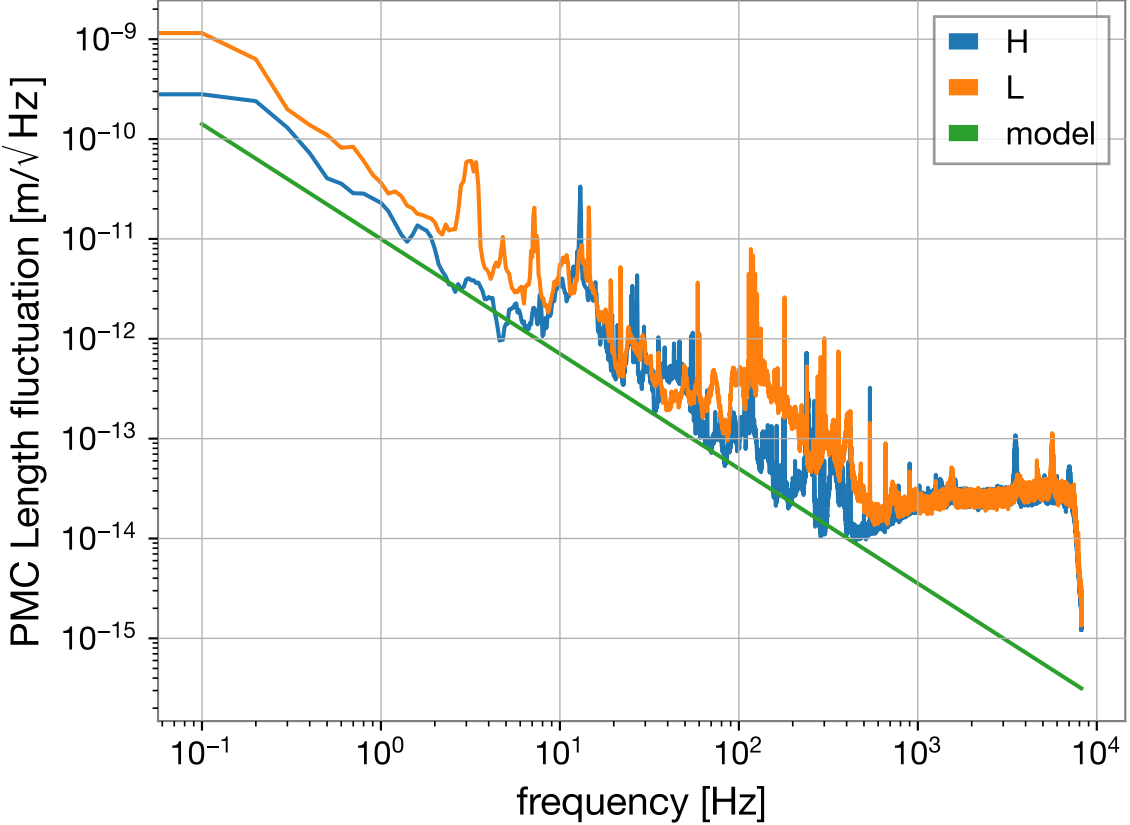


Figure 19: PMC length fluctuation of each site. This plot is using the data of L/H1:PSL-PMC_HV_MON_OUT_DQ from GPS time 1411790418 for 300 seconds. From these curves, the modeled JAC length motion is shown as solid green line.

an estimate for the PMC's length fluctuation. However, as the JAC will be placed on the ISI and in a vacuum, this estimation overstates the length fluctuation for the JAC, particularly in the audio frequency band where acoustic noise typically dominates. Additionally, above 300 Hz, the spectrum appears to be limited by sensing or actuator noise. Therefore, we modeled the JAC's expected length fluctuation as shown by the green solid line in Fig. 19.

Fig. 20 shows the spectrum of the signal obtained from the JAC reflection sensor, including length fluctuation, shot noise, PD noise [?], and ADC noise. The ADC noise was calculated assuming two-stage whitening. The shot noise is calculated by assuming 2% of mode-mismatching, which gives about 0.9 mW DC power at the REFL PD. As shown in the figure, the signal strength is sufficient. The noise budget of the length fluctuation suppressed by the designed servo is shown in Fig. 21.

5.1.6 Intensity noise due to residual length fluctuation

To evaluate whether the suppression provided by the designed control loop is sufficient, we assess the intensity noise caused by residual length fluctuations. Same as discussed in

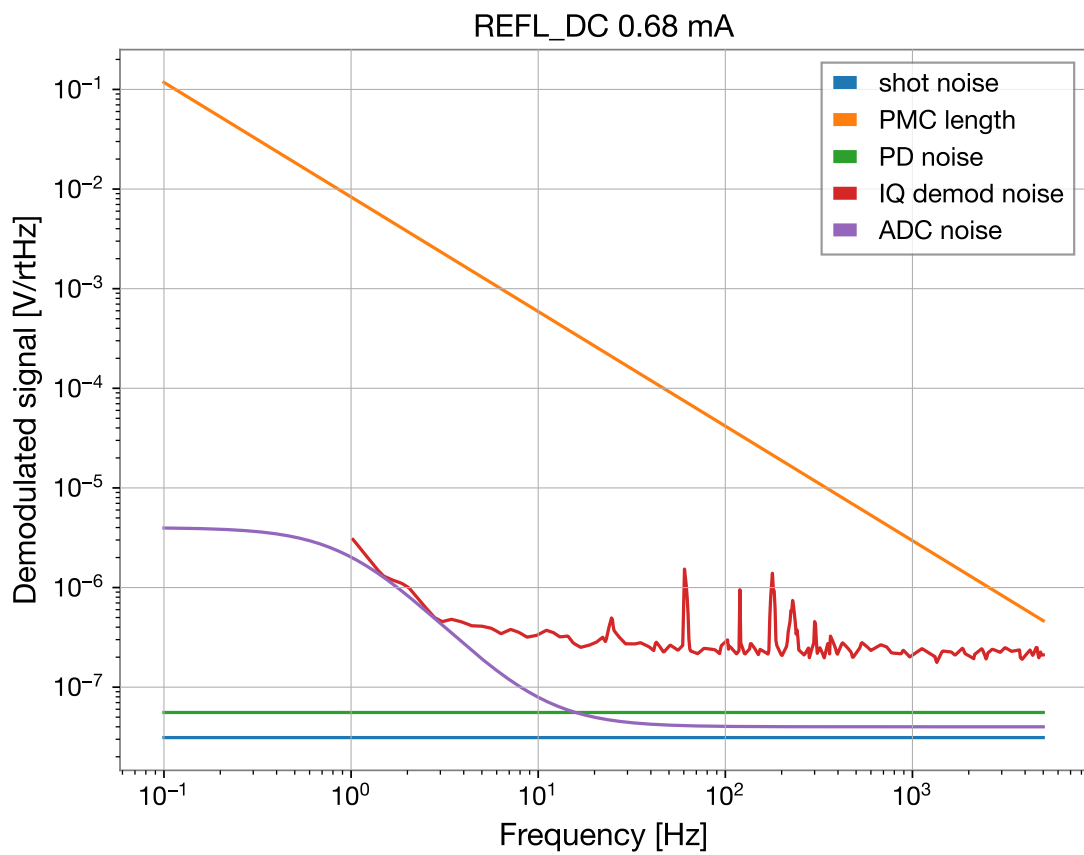


Figure 20: Expected error signal spectrum. For the shot noise calculation, 2% of mode-mismatching is assumed. The PD noise is calculated with 2 mA of shotnoise intercept current[?]. Demodulator and ADC noise refer [?], and two-stages of the whitening filter is assumed.

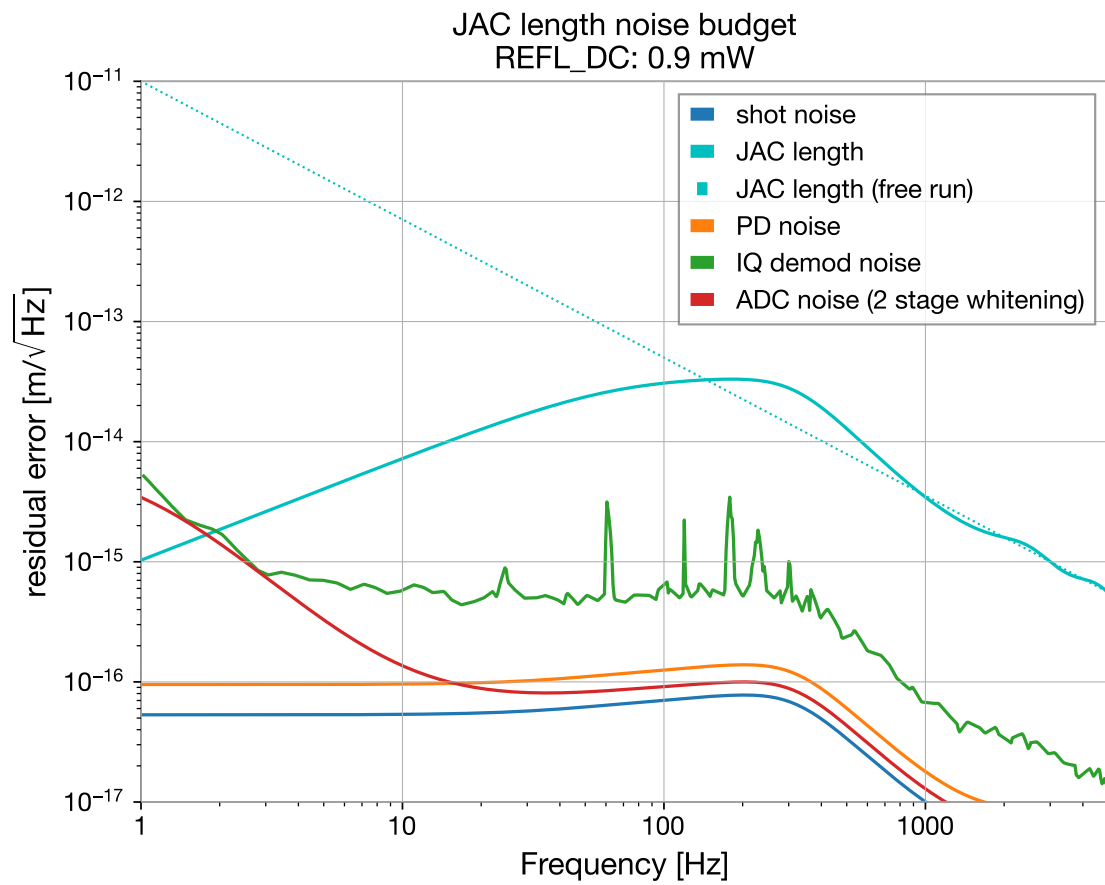


Figure 21: Noise budget of the residual length motion.

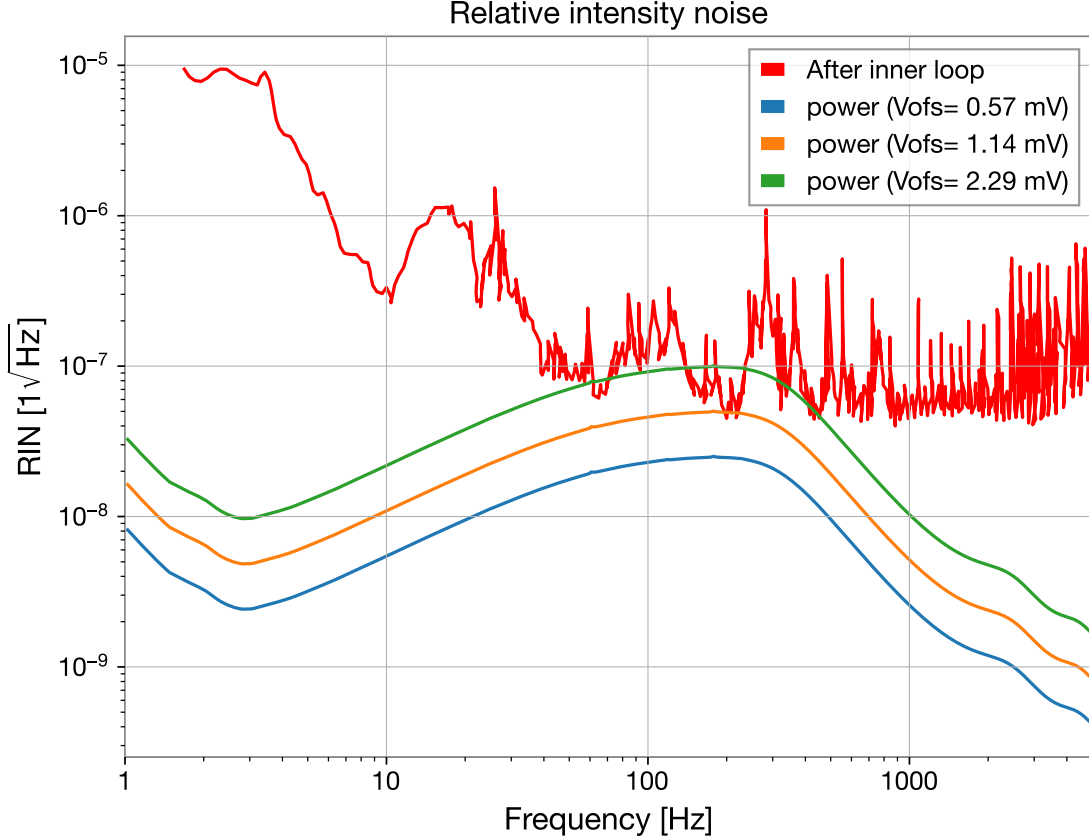


Figure 22: Expected relative intensity noise (RIN) caused by the residual JAC length motion. The current intensity noise stabilized by the ISS inner-loop is shown as red solid line [32].

Sec. 3.2, detuned cavities convert length fluctuations into intensity noise through the transfer function given similar to Eq. (8) as

$$\frac{dP}{d\xi} = 2\Delta\xi, \quad (12)$$

where $\Delta\xi$ is detuning normalized with HWHM. The HWHM in the unit of length is 2.1 nm. The previous calculation showed that length fluctuations are suppressed to below 3×10^{-14} m across all frequency ranges. Normalized to HWHM, this fluctuation corresponds to 1.5×10^{-5} . The intensity noise requirement for the JAC is to remain below the intensity noise stabilized by the current ISS inner loop, which is approximately 5×10^{-8} at 100 Hz as the relative intensity noise. From this, we derive that if the detuning of the cavity is less than $1.6 \times 10^{-3} \times$ HWHM, or equivalently, an offset of 1.1 mV in the demodulator output, then the output intensity noise would be comparable to the current residual intensity noise of the ISS inner loop.

Fig. 22 shows the expected intensity noise caused by length fluctuation with different offsets, along with the inner-loop-stabilized intensity noise measured at Hanford. As shown in the figure, intensity noise remains at acceptable levels if the offset drift stays below 2 mV.

5.1.7 Phase noise due to residual length fluctuation

The residual length noise will introduce phase noise into the output beam as well. The amplitude transmissivity of the critically coupled cavity is

$$t_{\text{cav}}(\xi) = \frac{1}{1 - i\xi} = \frac{1 + i\xi}{1 + \xi^2}, \quad (13)$$

where ξ is the residual length noise normalized by Half-Width-Half-Maximum (HWHM). Therefore, the phase noise of the output beam can be expressed as

$$\Delta\phi_{\text{out}} = \arctan \xi \simeq \xi. \quad (14)$$

A residual length fluctuation of 10^{-13} m will be converted into 4.7×10^{-5} rad of phase noise, which is equivalent to 4.7×10^{-3} Hz of frequency noise at 1 kHz.

Fig. 23 shows the estimated frequency noise caused by the residual length fluctuation of the JAC. The frequency noise will be suppressed by the CARM loop, and the suppressed frequency noise due to the JAC motion is also illustrated. This shows that the resulting frequency noise will be comparable to the current CARM residual noise.

5.1.8 Slow control

The JAC has two heaters of IS250C50RKE OHMITE. The slow drift of the cavity length (less than 0.1 Hz) will be offloaded to the JAC heater. During the conceptual design process, heat conduction to the table was considered as a potential issue, but we believe this will not pose a problem. The heater will maintain the JAC temperature, compensating for heating by the full laser power during lock acquisition. The expected use of the heater is as follows:

1. Lock the JAC with PZT at low power (about 1 W), and offload the DC control to the heater to keep the PZT input constant.
2. During lock acquisition, maintain this slow loop. As the heat from the laser increases with more input power, this loop will keep the JAC length stable by reducing the heater output.

As a result, the total heat on the JAC will remain constant during the lock acquisition. This control scheme allows the JAC heater to prevent changes in heat conduction to the ISI table.

5.1.9 Conclusion of the length control

For the length control, our design will include the following:

- Digital control.
- Bandwidth of 200 Hz.
- Required offset drift at I/Q demodulator less than 2 mV.
- 50 mW of power will be injected into the RF PD.
- The resulting equivalent intensity and frequency noise will be comparable to the current PSL output beam.

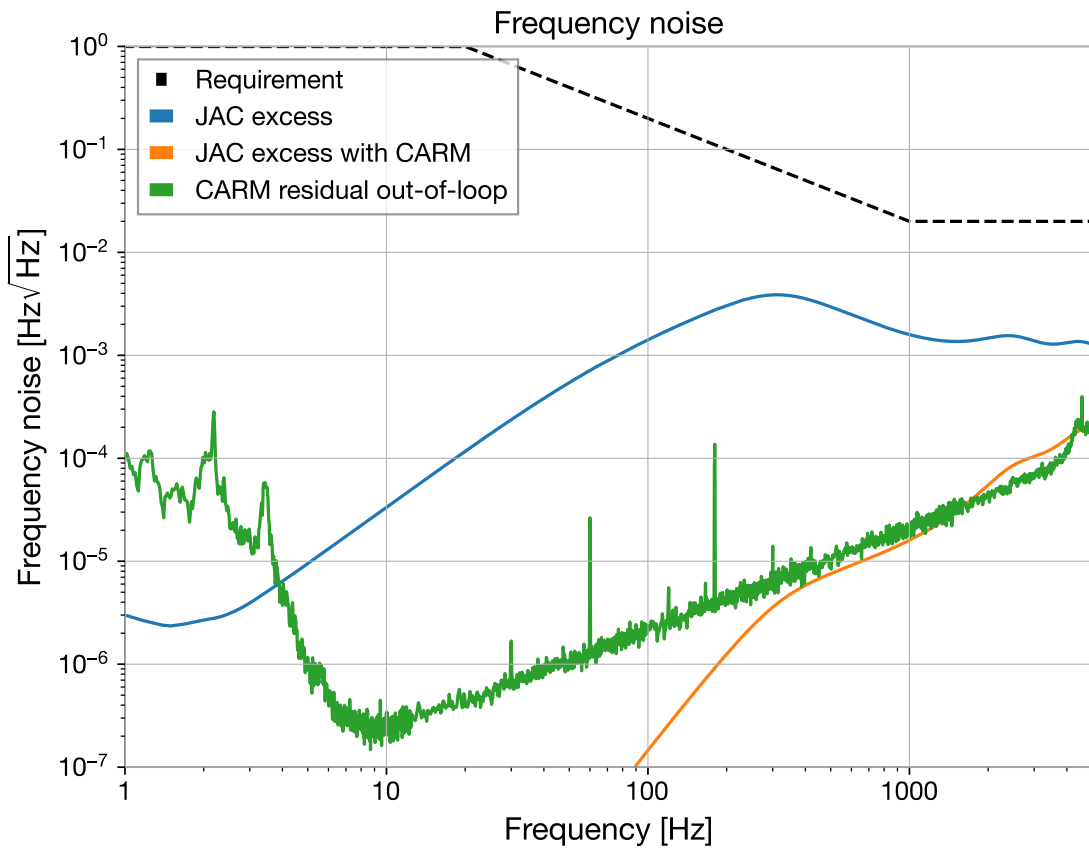


Figure 23: Frequency noise caused by the residual length noise of the JAC. The black dashed line shows the aLIGO FSS requirement [?]. Orange and green lines represent the frequency noise of the JAC output with and without the CARM loop, respectively. The CARM loop will reduce the output frequency noise to a level comparable to the current frequency noise of the input beam into the PRM.

5.2 Alignment control

TBD

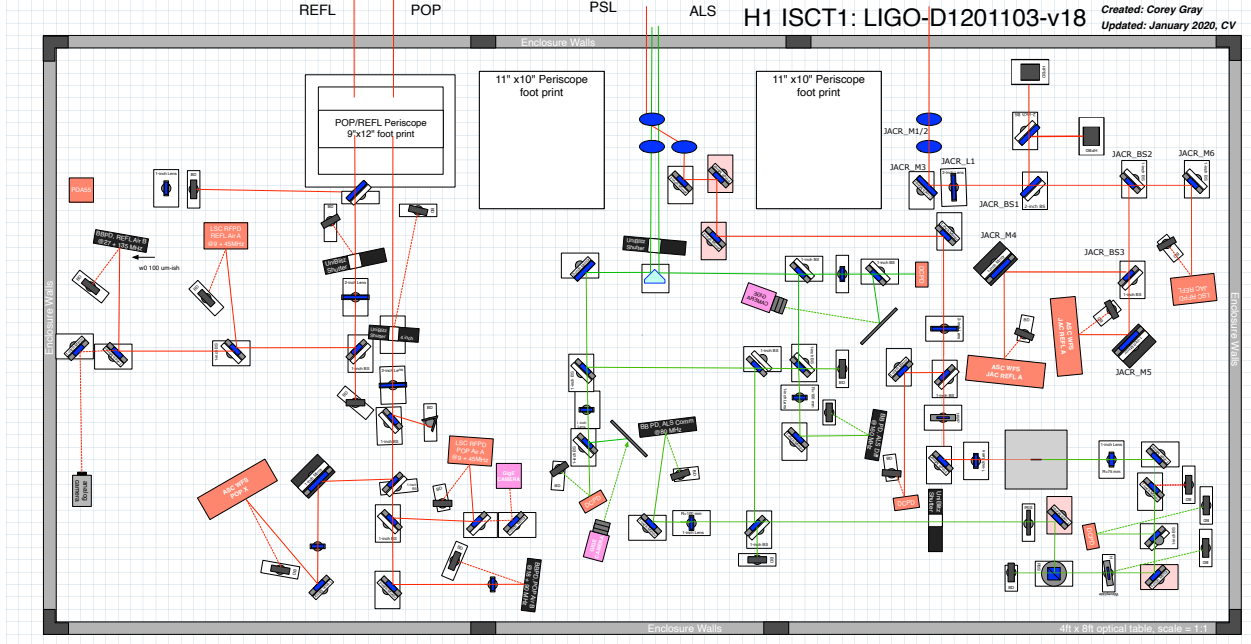


Figure 24: ISCT1 layout. The JAC reflected beam comes from the top right and is directed down by the third periscope.

6 In air table layout

The reflected beam from the JAC is directed to the ISCT1 table. The main components are the RFPD for length control and the WFSs for angular control. Additionally, a high-power beam dump is required. With this proposed layout, no changes are needed to the other REFL, POP, and ALS paths.

6.1 Layout

The ISCT1 layout design is shown in Fig. 24. The beam from the JAC reflection is directed downward by the periscope. The same periscope used for the ALS path will be utilized here. A picture and figure are shown in Fig. 26.

The first lens (JACR_L1) focuses the beam 0.7 m away from the lens with a beam radius of $625 \mu\text{m}$. The transmissivity of the first BS (JACR_BS1) is designed to be 1000 ppm, so it reflects most of the power to two beam dumps, as described in the following section. The second and third BSs are 50/50 BSs to split the power between the RFPD and WFSs for JAC length and angular control. Pico-motorized steering mirrors are located for the JAC WFSs to center the DC beam position on the WFSs.

6.2 Gouy phase telescope

The Gouy phase on the WFSs is optimized by the first lens. The beam propagation is shown in Fig. 25. The Gouy phase separation for the two WFSs is 90 degrees. Note that the distance between the chamber and the table is not measured but assumed, and there might

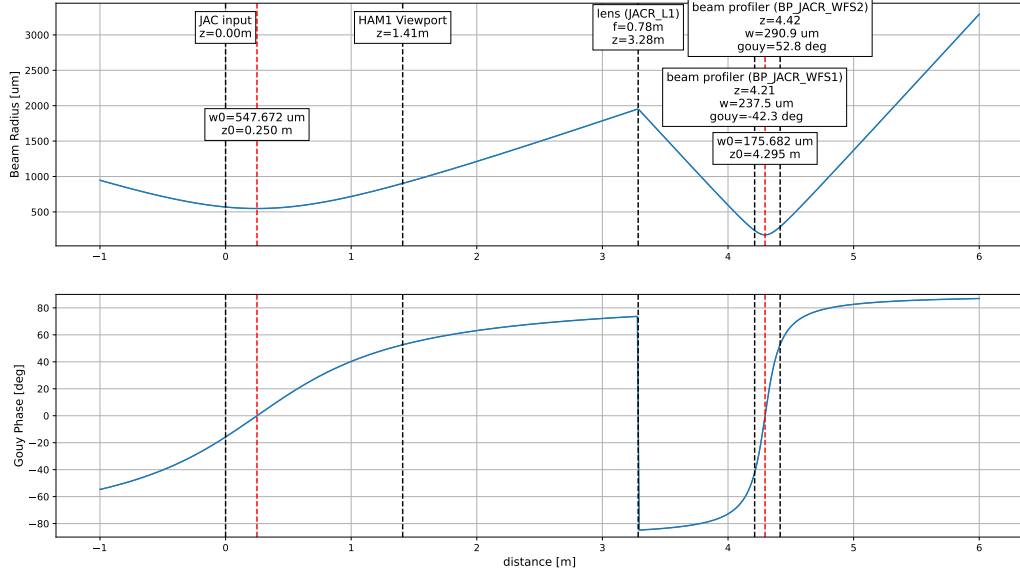


Figure 25: Beam propagation of the JAC reflection beam. JACR_L1 focuses and positions the beam waist between two WFSs.

be an error in the waist position. We will need to measure the beam propagation in-situ and may need to adjust the lens position.

6.3 High power beam dump

The beam dump needs to handle over 100 W of power. While there are several water-cooled beam dump options that can handle 100 W, we currently only have an 80 W-capable beam dump cooled with a heat sink. For the O5 upgrade, the plan is to use two 80 W beam dumps for the JAC. As a future upgrade, we should keep in mind the option to replace them with a water-cooled beam dump to handle more power with a single unit.

6.4 ALS Path

To ensure safety during installation work, the ALS path has been modified without changing its length. The ALS and JAC paths are well sectioned, and no beams overlap.

7 Risk Registry

7.1 JM misalignment

When the tip-tilt suspensions (JMs) are accidentally misaligned, the full-power beam may swing inside the chamber. If the motion is too large, the beam could hit and potentially

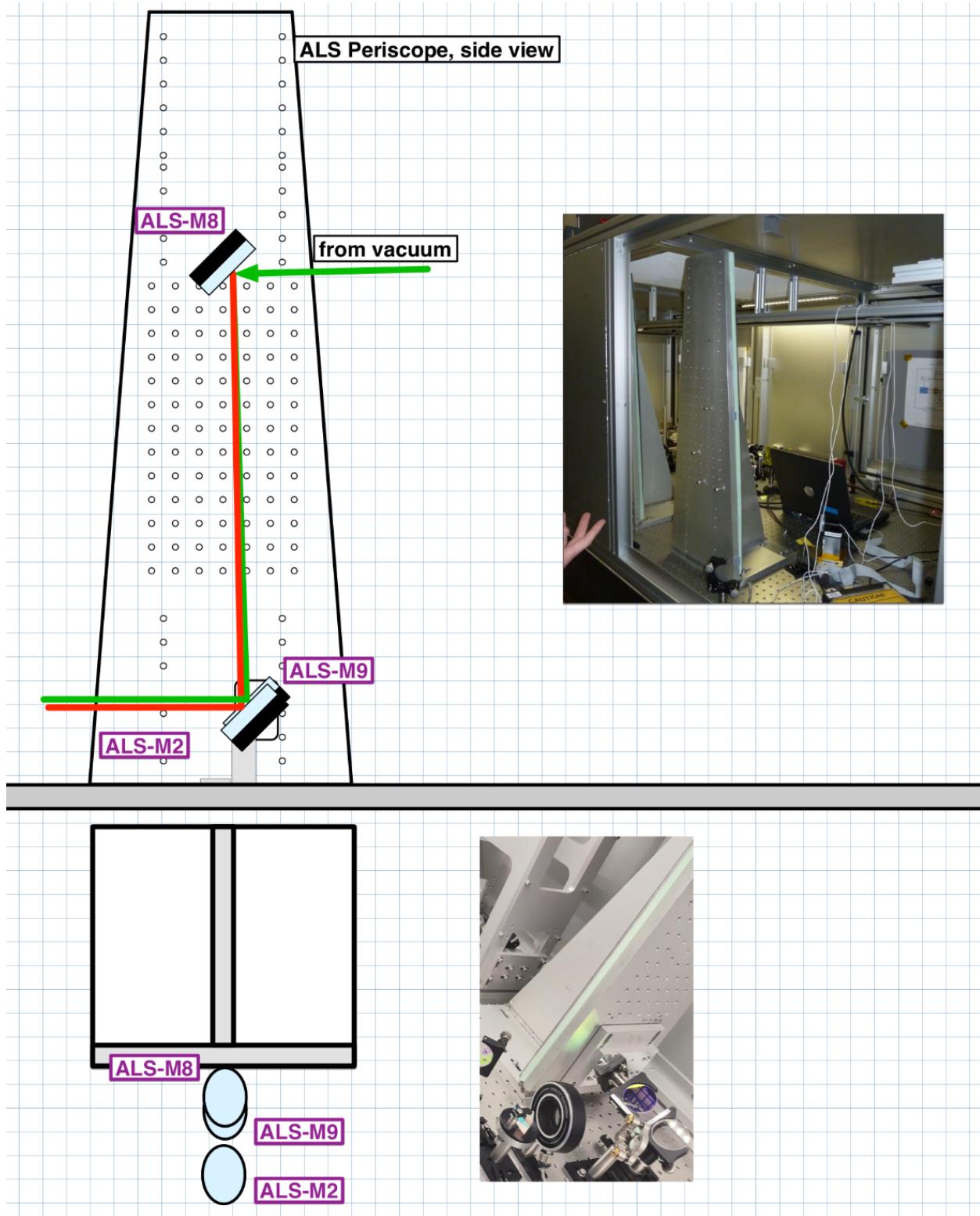


Figure 26: Periscope currently used for the ALS path on ISCT1.

damage in-chamber components. To evaluate this risk, the beam position motion at each optic as a function of JM misalignment is calculated.

The beam position motion can be described by the following equation:

$$\begin{pmatrix} x_{\text{out}} \\ \theta_{\text{out}} \end{pmatrix} = ABCD \begin{pmatrix} x_{\text{in}} \\ \theta_{\text{in}} \end{pmatrix} \quad (15)$$

where $ABCD$ is the ABCD matrix from the misaligned optic (acting as the motion source) to the optic of interest. Here, x and θ represent the beam position and propagation angle, while "in" and "out" indicate the moving optic and the optic of interest, respectively. Assuming the beam is centered on the misaligned optic, the beam position on the optic of interest can be calculated as:

$$x_{\text{out}} = B\theta_{\text{in}}. \quad (16)$$

Thus, the maximum angle at which the beam does not deviate from the optic can be calculated as:

$$\theta_{\max} = \frac{d \cos \theta_{\text{AOI}}}{B}, \quad (17)$$

where d is the diameter of the optic and θ_{AOI} is the angle of incidence.

As long as the misalignment of the mirror does not exceed this angle for all optics along the beam path to the beam dump, the beam will enter the beam dump properly and be dumped without issue.

JM1

JM1 is located before the JAC, and the beam will be reflected by the JAC input coupler and directed to ISCT1. The first BS on the ISCT1 (JACR_BS1) reflects most of the power, and the beam is directed to the beam dumps (JACR_BD1 and BD2). Therefore, we need to consider the path from JM1 to the JACR beam dumps (BDs) when evaluating the JM1 misalignment. There is one lens along this path (JACR_L1), so the ABCD matrix will differ after JACR_L1.

Before JACR_L1, the ABCD matrix is:

$$B = L \quad (18)$$

and after JACR_L1, it will be:

$$B = \left(1 - \frac{L_f}{f}\right) L + \frac{L_f^2}{f} = (-3.3 \times L + 14.3) \quad (19)$$

where L is the distance from the misaligned optic, f is the focal length of the lens, and L_f is the distance of the lens from the misaligned optic. The distances and the maximum allowable angles are shown in Table 2. The error is caused by position uncertainty, with all optics assumed to have a position error of 5 mm. The minimum allowance is for the beam dump and 3 mrad.

Optic Name	Distance (m)	Max Angle (degrees)
JAC input	0.2750	36.11(66)
JAC_M2	0.4550	31.56(35)
JACR_M1	2.6850	5.351(11)
JACR_M2	3.2410	4.4341(67)
JACR_L1	3.3299	6.127(29)
JACR_M3	3.4315	4.796(42)
JACR_BS1	3.5966	5.862(62)
JACR_BS4	3.7744	7.68(10)
JACR_BD	3.9268	3.206(55)

Table 2: Distances and maximum allowable angles for each optic.

JM2 and JM3

The beam reflected by JM2 and JM3 directes to HAM2 and reflected by input mirror of the IMC, and directed out to IOT1. We don't have no lens between JM2 and JM3, so the maximum allowance angle is always smaller for JM2 than JM3. Thus, we only show the calculation of JM2 here.

Optic Name	Distance from JM2 (m)	Max Angle JM2 (mrad)	Max Angle JM3 (mrad)
JAC_M4	2.1352	8.315 ± 0.017	14.417 ± 0.048
JAC_M5	2.3562	8.378 ± 0.015	12.847 ± 0.035
MCperi_t	3.8477	8.848 ± 0.012	7.401 ± 0.015
MCperi_b	4.0687	8.922 ± 0.013	6.964 ± 0.015
AROM RH1	4.2087	10.985 ± 0.018	8.219 ± 0.019
ROM RH1	4.4657	11.094 ± 0.020	7.710 ± 0.019
MC1 HR	4.7540	27.474 ± 0.064	17.656 ± 0.041
MCR_Per1_b	5.1709	9.310 ± 0.026	5.379 ± 0.013
MCR_Per1_t	5.2709	9.348 ± 0.026	5.270 ± 0.013
MCR_Per2_t	6.0209	9.633 ± 0.038	4.575 ± 0.012
MCR_Per2_b	6.1209	9.677 ± 0.037	4.496 ± 0.012
MCR_M1	8.5949	10.768 ± 0.087	3.1497 ± 0.0100
MCR_M2	9.1509	11.04 ± 0.11	2.9526 ± 0.0092
MCR_AR1	9.7069	11.34 ± 0.12	2.7764 ± 0.0088
MCR_M3	10.2629	11.65 ± 0.14	2.6219 ± 0.0087
MCR_M4	10.8189	11.98 ± 0.15	2.4820 ± 0.0078
MCR_BD1	11.3749	17.41 ± 0.24	3.335 ± 0.011
JAC_L2	1.2342	8.238 ± 0.029	46.3 ± 1.1
JAC_L3	1.9352	5.8445 ± 0.0100	11.478 ± 0.052

Table 3: Distances and maximum allowable angles for each optic.

8 Open questions

8.1 Thermal effect of the JAC

While the thermal lensing of the EOM has been verified to not pose a significant issue, the thermal effects of the JAC itself remain untested. As the input power changes from a few watts to over a hundred watts, the thermal conditions within the JAC will shift drastically. Although the heater will be used as part of the thermal compensation system, local thermal gradients, such as thermal lensing of the input or output mirrors and deformation of the JAC body, cannot be fully avoided. These effects may lead to changes in the output mode or alignment drift. Alignment compensation may be achievable through the tip-tilt suspensions, but if the available compensation range proves insufficient, it may be necessary to design an in-vacuum power adjustment stage.

8.2 Length fluctuation

The design calculations are based on assumed length fluctuations, estimated from the in-air PMC length fluctuations. However, it is possible that these assumptions underestimate the actual length fluctuations, leading to higher intensity and frequency noises in the output beam. During the testing phase, it will be necessary to evaluate the actual length fluctuation. If it is found to be larger than expected, we may need to increase the control bandwidth beyond the current design, potentially up to the kHz range. This could be achieved by switching from digital control to an analog servo system.

Related to the length fluctuation, the PMC is equipped with a damping structure designed to suppress body resonance. This structure utilizes Viton sheets, clamped from above, to apply force and mitigate resonant modes. It may require redesigning to improve performance and ensure compatibility with vacuum conditions.

9 Safety

9.1 Laser safety

In-chamber

For the JAC installation, alignment work can be done with a low-power laser. Before entering the chamber, ensure that the power from the PSL is sufficiently low (<100 mW).

Once the JAC is aligned and installed, a high-power test will also be required. Close all the flanges, monitor the inside of the chamber with a camera, and gradually increase the laser power.

Maintain the LVEA laser hazard status throughout the entire installation process.

ISCT1

We also need to align the ISCT1 table. As with the in-chamber work, the LVEA must be set as a laser hazard area. For the ISCT1 work, personnel must also be cautious of other beam paths, particularly the ALS-PSL path. This path is close to the JAC reflection path, and

the power exceeds 1 W. Therefore, it is recommended to conduct the work with an expert familiar with the ALS-PSL path.

10 Wiring

10.1 Analog circuit

The main circuit is the modulator and demodulator for the length and alignment sensing. These circuite will be located in PSL_R1, PSL_R2, ISC_R1, ISC_R2, ISC_R4. Also, for tip-tilt actuation, we place the coil driver on SUS_C4, and saterite box on SUS_R1. The rack layout is working in progress.

10.2 CDS

- The model will run in l/h1imc or make new model l/h1jac? -

10.3 HAM1 flange feedthrough

The main electronics in the HAM1 chamber related to the JAC will be

- 3 x Tip-tilt suspension
- JAC Controls (PZT, thermometer, and heater)
- DC PD
- EOM

Each tip-tilt needs a D25 connection for OSEM sensing and control. JAC PZT, JAC thermometer, heater, and DCPD will share a D25 cable. Therefore, four D25 connections are needed. The EOM has four electrodes, and each connection will use a coax cable.

Summarizing these cables, the required feedthroughs are:

- 2 x dual-D25: [D2000223](#)
- 1 x five-coax (Accuglass_25D-5CX-450): [D1600167](#)

11 Vacuum compatibility

11.1 Cavity

11.2 Electronics

12 Test plan

The test configuration is

12.1 Jitter attenuation

13 Installation plan

14

References

- [1] E. Capote, W. Jia, N. Aritomi, M. Nakano, V. Xu, and et al. Advanced ligo detector performance in the fourth observing run. *Phys. Rev. D*, 111:062002, Mar 2025.
- [2] aLOG 64098, 2023.
- [3] Daniel David Brown and Andreas Freise. Finesse. Technical report, May 2014. The software and source code is available at gwoptics.org/finesse.
- [4] aLIGO Tip-Tilt (HTTS) Mirror Assembly. [LIGO-D1001396-v3](#), 2010.
- [5] ALIGO IO H1 IN VACUUM PERISCOPE. [LIGO-D1201342-v5](#), 2012.
- [6] aLIGO, JAC, EOM, IN-VAC EOM ASSEMBLY. [LIGO-D2500130-v3](#), 2025.
- [7] ISCT1 Optical Layout. [LIGO-D1201103-v20](#), 2012.
- [8] aLIGO, JAC, IOT1. [LIGO-E2500019-x0](#), 2025.
- [9] LIGO aLOG Entry 39399. [LIGO aLOG Entry 39399](#), 2025.
- [10] 2" Lenses for the Jitter Attenuation Cavity. [LIGO-E2400437-v1](#), 2024.
- [11] Custom Optics: 1" lenses AR/AR 1064nm and 532nm. [LIGO-E2500026-v1](#), 2025.
- [12] ALIGO PSL TABLE LOCATIONS. [LIGO-T1000400-v1](#), 2010.
- [13] aLIGO Coordinate Systems. [LIGO-T0900340-v2](#), 2009.
- [14] ALIGO IO L1 MASTER COORDINATE LIST. [LIGO-E1200274-v3](#), 2012.
- [15] ALIGO IO H1 MASTER COORDINATE LIST. [LIGO-E1200616-v7](#), 2012.
- [16] Electro-optics for high power operation. [LIGO-G070376-x0](#), 2007.
- [17] alog84231, 2025.
- [18] alog76655, 2025.
- [19] aLIGO, high quality, .75 deg wedged, 6" Viewport Assembly. [LIGO-D1101000-v3](#), 2011.
- [20] Quotes for 2" BSs for the JAC upgrade post-O4. [LIGO-C2500078-v2](#), 2025.
- [21] Silicon (Si) Photodiode Circuit Board for FFD-200, GAP-5000 PDs. [LIGO-D1700116-v3](#), 2017.

- [22] LSC RFPD Assembly. [LIGO-E1900344-x0](#), 2019.
- [23] In-vacuum EOM design: Update. [LIGO-G1900329-v3](#), 2019.
- [24] RF Frequency Doubler Assembly. [LIGO-D1002178-v1](#), 2010.
- [25] C30642gh – ingaas pin, 2mm, to-5, 2021. Accessed: 2025-11-25.
- [26] aLIGO, ISC, RF System, 4 Channel I Q Demodulator. [LIGO-E1200112-x0](#), 2012.
- [27] Notes on RFPD Signal Chain Measurements. [LIGO-T1300315-v1](#), 2013.
- [28] aLIGO LSC RF photodetector test. [LIGO-G1101199-v1](#), 2011.
- [29] LIGO aLOG Entry 81385. [LIGO aLOG Entry 81385](#), 2025.
- [30] aLIGO, ISC, Electronics, PZT Driver with Dewhitening. [LIGO-E2500160-x0](#), 2025.
- [31] PZT Driver with Dewhitening Test Procedure. [LIGO-T2500269-v1](#), 2025.
- [32] ISS second loop requirements. [LIGO-T1600064-v2](#), 2016.